Chemical Engineering Journal Advances 5 (2021) 100080

Contents lists available at ScienceDirect

Chemical Engineering Journal Advances

journal homepage: www.elsevier.com/locate/ceja

Structure and activity of nickel supported on hibonite-type La-hexaaluminates synthesized from aluminum saline slags for the dry reforming of methane

J.J. Torrez-Herrera, S.A. Korili, A. Gil*

INAMAT˚2-Departamento de Ciencias, Edificio de los Acebos, Universidad Pública de Navarra, Campus de Arrosadía, E-31006 Pamplona, Spain

ARTICLE INFO

Keywords:
Aluminum industrial waste
Hexaaluminate synthesis from saline slags
Dry reforming of methane

ABSTRACT

This work describes the procedures followed to obtain four hibonite-type La-hexaaluminates (La-HA) using aluminum saline slag waste as the aluminum source. Briefly, an acid-extracted aluminum solution (8.9 g_{Al}/L) was used to synthesize the hexaaluminate by mixing with a stoichiometric amount of lanthanum nitrate and 2-propanol/polyethylene glycol/methanol/1-hexanol/glucose depending on the hydrothermal conditions of the synthesis. The results showed the formation of pure-phase hexaaluminate at 1473 K in all cases, with differences in the textural properties between the materials. The solids obtained were used as supports for nickel catalysts (10 wt.%) for the dry reforming of methane (DRM) at 973 K. The supports and catalysts were characterized by X-ray diffraction (XRD), N_2 adsorption at 77 K, X-ray fluorescence (XRF), temperature-programmed reduction (TPR), scanning electron microscopy (SEM) and transmission electron microscopy (HR-TEM). An effect of the textural properties, dispersion of the metallic phase and nickel-support interaction on the performance of the catalyst was found. Our results also show a new application of a catalyst synthesized from an industrial waste such as aluminum saline slags.

1. Introduction

In recent years, there has been a disproportionate increase in the concentrations of greenhouse gasses (GHG) present in the Earth's atmosphere. Methane and carbon dioxide are major greenhouse gasses and appear to make important contributions to climate change as their concentrations have increased by approximately 253% and 143%, respectively [1–3]. Almost all options for methane transformation involve its initial conversion into synthesis gas (CO + H_2). Moreover, there is a renewed interest in the chemistry of C1 sources, and the large-scale conversion of natural gas into liquid fuels has created a need to explore new methods for reforming natural gas.

Dry reforming of methane (DRM) offers an alternative to reduce the impact of these gasses and produce clean energy sources and other derived products, therefore this process has gained a lot of attention recently. Among the different reforming processes available, dry reforming ($CH_4 + CO_2 \rightleftharpoons 2CO + 2H_2$) could represent a very interesting approach to adding value to an inexpensive source of carbon (CO_2) and reducing the overall carbon emissions associated with the increase of world consumption of methane of fossil origin. The production of synthesis gas (CO + H_2) for various applications [4–6] could also be considered as an interesting method related to DRM.

DRM produces an H_2/CO molar ratio of 1, thus making it the most convenient for Fisher-Tropchs synthesis when compared to steam reforming (H_2/CO=3) and partial oxidation (H_2/CO=2). DRM is affected by several parallel reactions that occur in the process, including the decomposition of methane (Eq. (2)), the reverse water-gas shift reaction (RWGS, Eq. (3)), the Boudouard reaction (Eq. (4)), CO_2 hydrogenation (Eq. (5)), CO hydrogenation (Eq. (6)) and steam reforming (Eq. (7)) [7,8].

$$CH_4 \rightleftharpoons C + 2H_2 \quad (2)$$

$$CO_2 + H_2 \rightleftharpoons CO + H_2O \quad (3)$$

$$2CO \rightleftharpoons C + CO_2 \quad (4)$$

$$CO_2 + 2H_2 \rightleftharpoons C + 2H_2O \quad (5)$$

$$H_2 + CO \rightleftharpoons H_2O + C \quad (6)$$

$$CH_4 + H_2O \rightleftharpoons CO + 3H_2 \quad (7)$$

When the system is led by Eq. (3), the selectivity with respect to H_2/CO can be lower than 1, and the deposition of coke could be led by Eqs. (4)–(6) [9].

* Corresponding author.
E-mail address: andoni@unavarra.es (A. Gil).

https://doi.org/10.1016/j.ceja.2020.100080
Received 6 November 2020; Received in revised form 27 December 2020; Accepted 28 December 2020

If a stoichiometric ratio of CO_2 and CH_4 is used in DRM, the conversions of both gasses could be expected to be equal and therefore the production of synthesis gas should be equal to unity. The presence or dominance of the RWGS reaction can be confirmed at the reactor outlet by the production of H_2O (g) and a much higher stoichiometric conversion of CO_2 than CH_4, and the Boudouard deprotonation can be confirmed by an increase in CO formation. An increase in CH_4 conversion into CO_2 is an indication of CH_4 decomposition [7,10]. Coke formation in the catalyst is an undesirable side reaction that has a negative effect, since it blocks and encapsulates the active sites and support. This undesired reaction can be controlled by combining the hydrogenation reactions of CO_2 and CO with the RWGS reaction [9,11,12].

The catalysts used in DRM are usually based on noble metals (Ru, Rh, Pt) or transition metals (Ni, Co) as the active phase. Noble metals have been shown to be more active and more resistant to coking compared to Ni or Co at equal particle sizes and dispersions, but have the great disadvantage of low availability and high cost, which means that Ni tends be used as the preferred metal for the production of catalysts on an industrial scale [13,14].

Hexaaluminates are a family of hexagonal aluminate compounds with unique layered structures consisting of alternating spinel blocks with closed packages of oxide ions and mirror planes. The general formula is $AB_xAl_{12-x}O_{19}$, where *A* is typically a large, mono-, di-, or trivalent cation present in the mirror plane. Some examples of *A* include Na, Ba, La, Ca, Sr, and Ce, amongst others. Component *B* represents a transition metal (Mn, Fe, Co, Cu, Ni, etc.) or noble metal ion (Ir, Ru, Pd, Rh), which can partially or completely replace the Al positions in the crystallographic structure [15–17]. Hexaaluminates comprise a spinel block and a mirror plane stacked alternately to form a kind of layer structure. The spinel blocks comprise only Al^{3+} and O^{2-} ions, and have the same rigid structure as spinel. Large cations such as Na^+, K^+, Ba^{2+}, Ca^{2+}, Rb^{2+}, Sr^{2+}, and La^{3+} are located in the spacious mirror plane. Depending on the charge and radius of the large cations in the mirror plane, hexaaluminates have a β-Al_2O_3 (hibonite) or magnetoplumbite (MP)-type structure that can ideally be represented as $MAl_{11}O_{17}$ and $MAl_{12}O_{19}$, respectively [18]. Catalysts based on hexaaluminates as the support and nickel as active phase are of great interest in high temperature catalytic reactions due to their marked thermal stability and resistance to sintering [15,19]. Structural substitution with other metals, including nickel, improves catalytic activity, whereas cations such as La^{3+}, prevent inactivation [20,21].

Various methods of hexaaluminates have been presented by several authors and reviewed by our group recently [22]: solid state reaction, sol-gel, co-precipitation, reverse microemulsion, nitrate decomposition, hydrothermal synthesis, carbon template, freeze drying, among others. The decomposition of nitrates is a simple method, since it consists of adding the aqueous solutions of the salts to a mixture of 2-propanol/polyethylene glycol/methanol/1-hexanol/glucose, after a reaction time, which may be under pressure, the drying and calcination steps are continued. Based in this general method, the synthesis of hexaaluminates from an aluminum solution extracted from saline slag wastes is reported in this work.

Saline slags are generated during secondary aluminum processes, i.e. aluminum recycling. These slags comprise metallic aluminum, several oxides, and flux brines as principal components, with variations in the percentage of non-metallic products that depend on the nature of the material being recycled [23]. The difference in composition makes it difficult to develop a standard recovery method, and waste is nowadays mainly stored in controlled landfills. In this context, some materials, for example alumina [24–27], calcium aluminate [28–30], layered double hydroxides (LDHs) [31–35], microporous aluminophosphate molecular sieves [36,37] and zeolites [38–42], synthesized from this type of waste have been described by various authors. To the best of our knowledge, valorized materials such as hexaaluminates have never been synthesized from aluminum saline slags and tested as a support for metal catalysts in the dry reforming reaction.

In this work, the synthesis, characterization and evaluation of hibonite-type Ni/La-hexaaluminate catalysts was carried out in order to valorize a high impact industrial waste derived from the secondary aluminum manufacturing industry, with the aim of evaluating their structure, activity and stability during a reaction period of at least 20 h.

2. Experimental

2.1. Materials, reagents, gasses and aluminum extraction

The materials and reagents used for the synthesis of hexaaluminates and catalysts included lanthanum(III) chloride heptahydrate (99.9%, Sigma-Aldrich), 2-propanol (99.5%, Sigma-Aldrich), polyethylene glycol 400 (Merck), polyethylene glycol Monolaurate 400 (PegMn400, Aldrich), methanol (99.8%, Emparta ACS), 1-hexanol (98%, Sigma Aldrich), D(+)-glucose (99.5%, Sigma Aldrich) and $Ni(NO_3)_2 \bullet 6H_2O$ (PA, Panreac). Carbon dioxide (99.996%, Praxair), helium (99.999%, Praxair), hydrogen (99.999%, Praxair), methane (99.5%, Praxair) and nitrogen (99.999%, Praxair) were also used.

Aluminum was extracted from saline slags using the following procedure: 50 g of saline slag was added to 750 mL of an aqueous reagent solution (HCl, 2 mol/L) in a reflux system consisting of a 1000 mL erlenmeyer flask with tube condenser, thus avoiding volume losses. The slurries were heated to 373 K and kept at that temperature for 2 h. The solution was then allowed to cool and separated by centrifugation. The most important constituents of the filtered solution were determined by ICP-OES, using a VARIAN ICP-OES VISTA MPX with radial vision. The results obtained are summarized in Table S1. The composition of the separated powder (see Table S2) was determined semi-quantitatively by X-ray fluorescence (XRF) using a PANalytical AXIOS instrument.

2.2. Catalyst preparation

Hexaaluminate synthesis was performed using four methods, with a La/Al molar ratio of 1:11. The final mixture obtained was heated in a stainless steel autoclave at 473 K for 16 h, dried in an oven until the liquid matrix had been removed, then calcinated at 673 K for 1 h and 1473 K for 2 h, in both cases using a heating ramp of 10 K/min.

2.2.1. Method 1: Alcohol Dilution (AD)

The extracted aluminum solution was heated to reduce its volume fivefold, thus giving a concentrated solution for hexaaluminate synthesis. Lanthanum chloride was dissolved in a mixture of isopropanol/polyethylene glycol in a 1/1 volumetric ratio. The mixture of alcohols was then added to the aluminum solution slowly, with vigorous stirring, over 30 min, then poured into a 250 mL stainless steel autoclave reactor and heated at 473 K for 16 h. The resulting product was dried in an oven until the liquid matrix had been eliminated, then calcinated at a heating rate of 10 K/min to 673 K for 1 h, and then successively to several temperatures between 873 and 1473 K for 2 h to study the structure evolution.

2.2.2. Method 2: Modified Alcohol Dilution (MAD)

In this case, a mixture of alcohols (isopropanol/polyethyleneglycol/ethylene glycol, volume ratio 2/1/0.5) and D(+)-glucose was used. The lanthanum chloride was dissolved in isopropropanol, with vigorous stirring, then the concentrated aluminum solution was slowly added and the mixture left to stand at 333 K for 10 min. Glucose (10 g) was then added and the mixture stirred for an additional 20 min at the same temperature. Finally, ethylene glycol and polyethylene glycol were added slowly, maintaining the same conditions for 20 min, then the mixture was poured into a 250 mL stainless steel autoclave reactor and heated at 473 K for 16 h. The resulting product was dried in an oven until the liquid matrix had been eliminated, calcinated at a heating rate of 10 K/min to 673 K for 1 h, and then successively to several temperatures between 873 and 1473 K for 2 h to study the structure evolution.

2.2.3. Method 3: Modified Alcohol Dilution with Pegmn (MAD+PegMn)

The procedure used was similar to MAD with the incorporation of polyethylene glycol monolaurate 400 for the formation of a multicomponent mixture isopropanol/polyethyleneglycol/PegMn400, with a 2/1/0.5/0.5 volumetric ratio, maintaining the same procedure and conditions.

2.2.4. Method 4: Reverse Microemulsion with Alcohol Dilution (RMAD)

This method involves the formation of a reverse microelmulsion using methanol/polyethyleneglycol/PegMn400/hexanol/aluminum solution in a 1/0.9/0.5/1.5/0.6 volumetric ratio. First, lanthanum chloride was dissolved in the aluminum solution at 353 K, with vigorous stirring. After 10 min, methanol and hexanol were added slowly, stirring the mixture for a further 10 min, then polyethyleneglycol and PegMn400 were added. The temperature was increased to 373 K and the mixture maintained under these conditions for 20 min before digestion in the autoclave reactor as described in the previous procedures.

The samples synthesized above were denoted as *S1-AD, S2-MAD, S3-MAD+PegMn and S4-RMAD.*

The catalysts were prepared by wet impregnation of the synthesized hexaaluminate supports using nickel solutions to obtain a nominal 10 wt.% of Ni in all cases. The impregnated solids were then dried at 373 K for 16 h and calcined at 673 K for 2 h. The synthesized catalysts were denoted as *S1, S2, S3* and *S4*, without taking into account the acronym of the method used to prepare the support.

2.3. Characterization techniques

The structural phases were analyzed using an X-ray diffractometer (model Siemens D5000) equipped with an Ni-filtered CuKα radiation source (λ= 0.1548 nm). The crystallite size was determined from the experimental diffractograms using the Debye-Scherrer equation. The main textural properties of the solids were determined by nitrogen adsorption at 77 K using a Micromeritics ASAP 2020 Plus adsorption analyzer. Prior to the adsorption measurements, 0.3 g of sample was degassed at 473 K for 2 h at pressures lower than 0.133 Pa. The BET surface area (S_{BET}) was calculated from adsorption data obtained over the relative pressure range 0.05–0.20. The total pore volume (V_P) was calculated from the amount of nitrogen adsorbed at a relative pressure of 0.99. The chemical composition of the sample was determined semiquantitatively by X-ray fluorescence (XRF) using a PANalytical AXIOS instrument. Temperature-programmed reduction (TPR) studies were performed using a Micromeritics TPR/TPD 2900 equipment instrument. TPR tests were then carried out from room temperature to 1273 K under a total flow of 30 mL/min (5% H_2 in Ar, Praxair). Finally, the morphological analysis and chemical composition of the samples were carried out using a SEM Phenom XL desktop (Mode: 15 kV - Map, Detector: BSD Full) and HR-TEM (JEOL JEM 2100F, Accelerating voltage: 200 kV, Detector: X-Max).

2.4. Catalytic performance

The dry reforming of methane (DRM) was carried out using an automated bench-scale catalytic unit (Microactivity Reference, PID Eng&Tech) at 973 K. The reactor was a tubular, fixed-bed, downflow type, with an internal diameter of 0.9 cm and a length of 30 cm. Catalyst samples (25 mg) were mixed with an inert material (SiC, VWV Chemicals-Prolabo) to dilute the catalyst bed and avoid hot spot formation. The reaction mixture consisted of CH_4 and CO_2 with a molar ratio of 1:1 (concentration of 12% in the feed), with helium as equilibrium gas up to a total feed flow of 40 mL/min, thus achieving a gas high spatial velocity (GHSV) of 9.6×10^4 mL/g h. Before the reaction, the catalyst was reduced *in situ* using 30 mL/min of H_2 at 973 K for 2 h. The reagent and product streams were analyzed using an Agilent 6890 gas chromatography system.

3. Results and discussion

3.1. Support characterization

3.1.1. X-ray difraction

The materials synthesized using aluminum extracted from saline slags, and calcined at 1473 K, were characterized by XRD and the patterns obtained are shown in Fig. 1. A very complex diffractograms have been obtained. Based on the extraction of multimetal oxides, and the presence of La and Ca, the most probable hexaaluminate structure, and that which best fits the existing patterns, appears to be magnetoplumbite. Indeed, hibonite-Ca (pattern # 00-007-0785), which is a type of magnetoplumbite, is the structure in closest agreement with the synthesized samples. The hexaaluminates (hibonite-La) obtained using the different methods present crystalline characteristics and different phases. For example, Fig. 1-A (sample *S1-AD*) shows a high crystallinity with narrow and high intensity peaks in which the hexaaluminate phase is practically pure. The maximum peak is obtained between 66° and 68° (2ɵ), almost entirely coinciding with the aforementioned pattern. Fig. 1-B (sample *S2-MAD*) shows a very similar crystalline behavior to that of Fig. 1-A, with an enriched hexaaluminate phase exhibiting narrow and well-defined peaks. In the case of Fig. 1-C (sample *S3-MAD+PegMn*), a reduction in the height of the main peak in the hibonite pattern at 67.3° is observed. This peak widens and merges with the spinel peak. The correspondence with a spinel peak at 37.2° can also be seen. As such, mixed phases can also be seen in the sample, although it has a lower content of the hexaaluminate phase than sample *S1-AD*. In the case of sample *S4-RMAD* (see Fig. 1-D), the appearance of the peak with greater intensity at 67.3° can also be seen, although in this case it is broader than in the patterns for samples *S1-AD, S2-MAD* and narrower than in sample *S3-MAD+PegMn*, therefore a majority hexaaluminate phase can be assumed.

3.1.2. Chemical composition and textural properties of the supports

The semiquantitative composition of sample *S1-AD* was determined by X-ray fluorescence (low limits of detection for major elements are in the range of 0.01 wt.% and approximately 10 ppm for trace elements, see Table S3). These results allow us to establish a general formula for the synthesized hexaaluminate assuming that this oxide, with a β-Al_2O_3 (hibonite) type structure, is only obtained in the final sample, as shown:

$$\left(Ca_{0.54}Na_{0.67}La_{1.08}\right)\left(Si_{1.32}Mg_{0.83}Fe_{0.18}Mn_{0.02}Ti_{0.03}\right)Al_{9.06}O_{19-\delta}$$

The specific surface (S_{BET}), pore volume (Vp) and pore diameter (dp) are summarized in Table 1, which clearly shows a direct effect of the synthesis method on these parameters. Thus, the RMAD method (sample *S4-RMAD*) favors an increase in S_{BET} but reduces the crystallinity of the sample, giving a larger pore volume and a smaller crystallite size than the remaining methods. This behavior may be due to microdrop encapsulation during synthesis in the liquid matrix, which allows a reasonable porosity to be maintained at 1473 K but reduces the crystallinity and purity of the sample with respect to that obtained using the AD method. This latter method (sample *S1-AD*), in turn, leads to a practically pure hexaaluminate phase with high crystallinity but an almost zero S_{BET} value, which can be explained by agglomeration of the microcrystals produced by the PEG400/ethylene glycol ratio used [43,44]. This method of preparation generates a particular adhesion effect, thus resulting in significant densification and a larger crystallite size compared to other samples. The synergy of the saline slag components, high solid state diffusion and low porosity can produce transformations to the hexaaluminate phase between 1273 and 1373 K and a rich phase (high purity) at 1473 K. Pure La-hexaaluminate exhibit a double Frenkel defect, which hinders formation of the hexaaluminate phase with a molar La:Al ratio of 1:11, This defect can be corrected if the amount of aluminum is increased to around 14–15 with respect to lanthanum. As such, a predominant hexaaluminate phase can be obtained, with an aluminate phase as a secondary, although not pure, phase even increasing the calci-

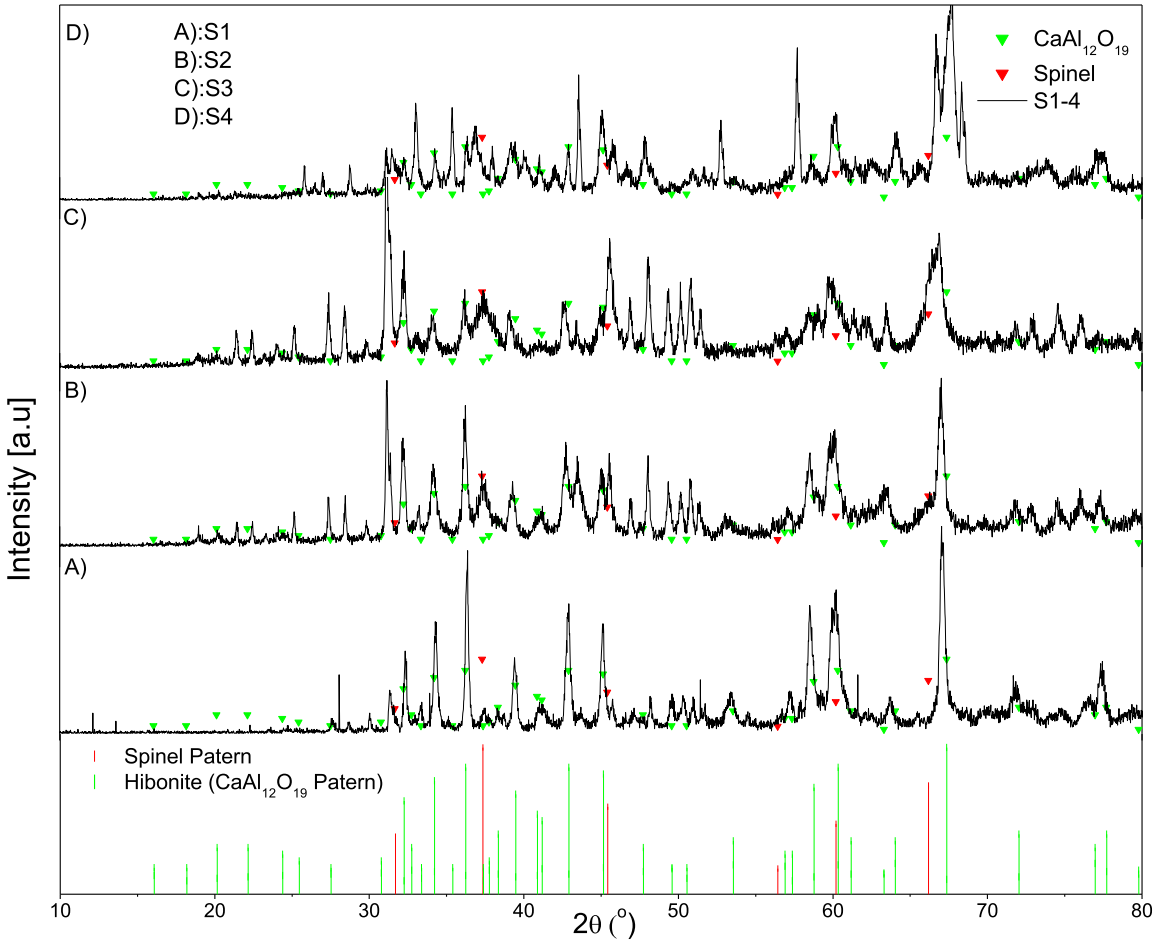

Fig. 1. XRD patterns of the hexaaluminates synthesized using La and Al extracted from saline slags (the hibonite and spinel patterns are included for comparison). Symbols: ▼ Spinel pattern #00–021–1152, ▼ Hibonite pattern #00-007-0785.

Table 1
Specific surface area, pore volume, pore diameter and crystallite size of the samples synthesized. The structure of the predominant phase is also included.

Sample	Method	S_{BET} (m^2/g)	Vp (cm^3/g)	dp (nm)	Cristallite Size (nm)		Phase structure
					LaHA	NiO (mean)	
S4	RMAD	30	0.198	38	6	20	HA >>Spinel
S3	MAD+PegMn	21	0.056	20	8	16	HA > >Spinel
S2	MAD	12	0.034	17	19	14	HA >>Spinel
S1	AD	1	0.003	10	25	16	HA

nation temperature to 1723 K [45,46]. In the case of the hexaaluminate obtained from the saline slags, the aluminum solutions self-corrects the double Frenkel structural defect. A stoichiometric ratio, and the metallic synergy of the components, makes it possible to obtain the hexaaluminate phase at lower calcination temperatures. This can be due to the fact that a lower diffusion energy is needed in the solid-state reaction in the presence of other metals.

The sample *S3-MAD+PegMn* shows a higher S_{BET} value than the *S1-AD* and *S2-MAD* samples. The separation effect produced by the carbonization of glucose within the matrix, which is maintained up to 973 K, and the dispersive-surfactant effect of PEG400-PEG400Mn allow the separation of the crystals and the porosity to be maintained during the calcination process. With respect to the MAD method (sample *S2-MAD*), the effect of adding glucose is remarkable, since this substance forms a carbonaceous matrix that allows the separation of the nanocrystals formed to be maintained while reducing their porosity by adhesion in a similar manner to that found for sample *S-AD*. Finally, it should be mentioned that an excellent crystallinity and sample purity is achieved.

3.1.3. TPR analysis

A TPR analysis of the supports was carried out to verify that the metals present during the synthesis were fully incorporated into the internal structure of the hibonite. An absence of peaks was found.

3.2. Catalyst characterization

3.2.1. X-ray difraction

The NiO/La-hibonite catalysts were characterized before being tested in the DRM reaction. The diffractograms presented in Fig. 2 (top) show the structural stability of the samples after impregnation; the peaks corresponding to the standard can also be seen. The lower part of this figure shows a superposition of the diffractograms for the support and the catalyst, thus allowing the peaks to be identified more easily.

After impregnation with nickel, the hexaaluminate structure of the support remains perfectly stable and the presence of NiO is also detected (peaks at 37.2°, 43.3° and 62.8°). The patterns of the identified oxides were uniformity in all cases since very similar peak intensities are

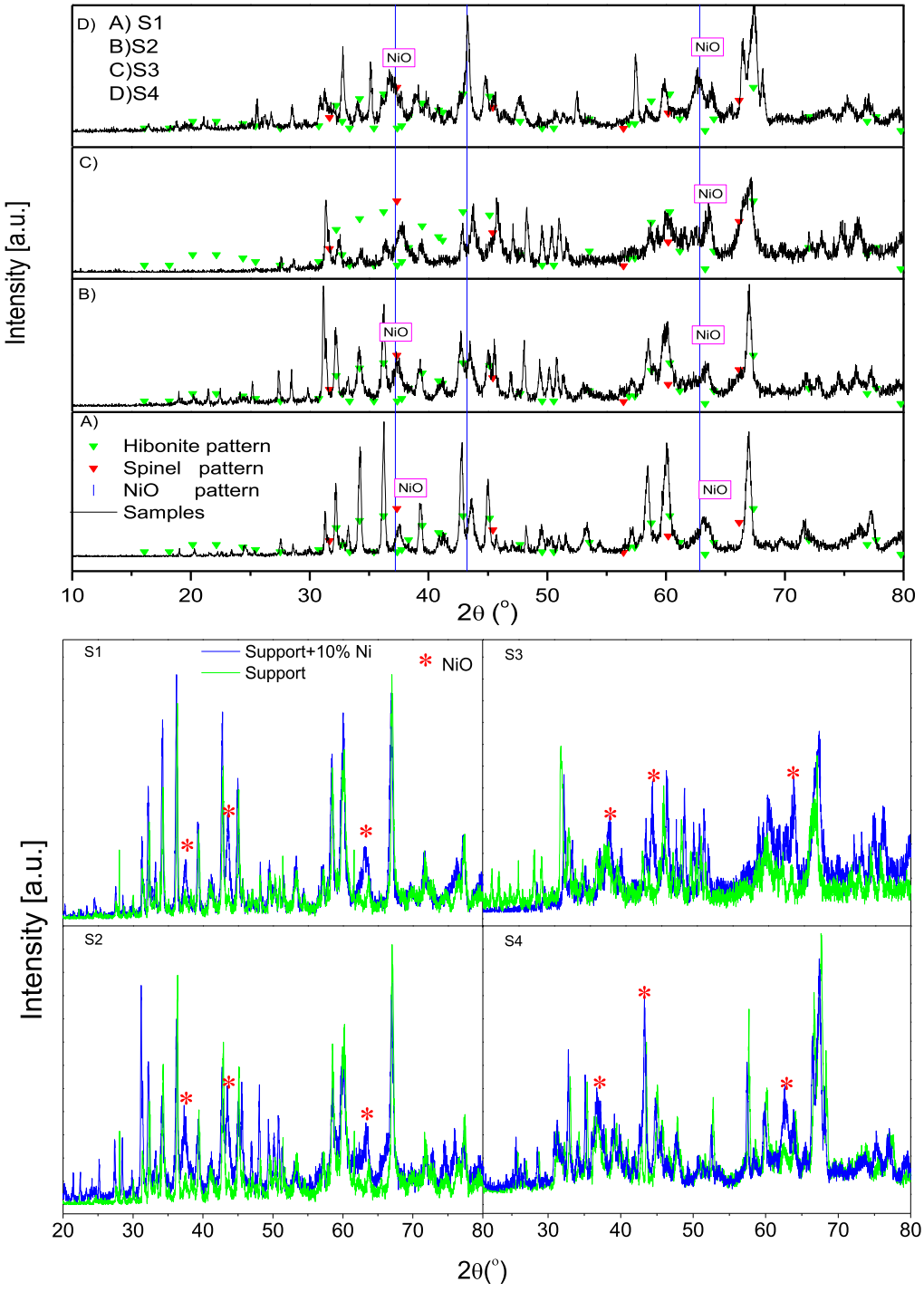

Fig. 2. (Top) XRD pattern of the Ni/hexaaluminate synthesized using La and Al extracted from saline slags (the hibonite, NiO and spinel patterns are included for comparison). (Bottom) Comparison between support and catalyst. Symbols: ▼ Spinel pattern #00-021-1152, ▼ Hibonite pattern #00-007-0785, | NiO pattern #01-073-1523.

present, despite the differences in porosity and crystallinity of the supports. The average crystallite size for nickel oxides is included in Table 1, which shows that the average value for all samples post-impregnation was 14 nm, as determined by XRD. This result suggests that growth of the crystal during the sintering process was similar in all catalysts. Consequently, the increase in specific surface area of the support does not significantly affect the sintering process of nickel crystals during calcination. To explain these results, it must be taken into account that the supports are characterized as materials with very low porosity that will prevent the dispersion of the metallic species. Therefore, larger oxide particles will predominate, particles that are of greater importance when the Debye-Scherrer equation is used to determine the crystallite size. Similarly, it is necessary to take also into account how the measurement of the specific surface areas is carried out and how the samples are prepared by wet impregnation in order to understand the differences obtained. The specific surface areas are determined by adsorption of N_2 at 77 K, where previously the materials have been treated at high vacuum. The impregnation with the Ni (II) solution is carried out using an aqueous solution with a high metal content, it being difficult to produce a dispersion at the atomic level of Ni (II).

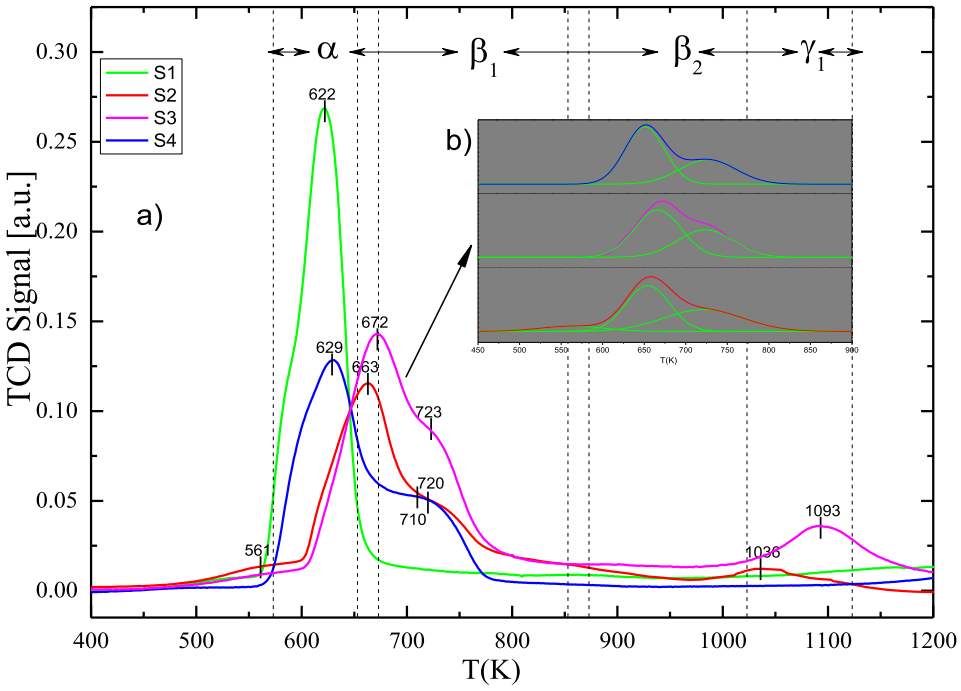

Fig. 3. a) TPR patterns of the NiO/hexaaluminate samples for the four methods, all samples were calcined at 1473 K. b) Peak deconvolution for *S4, S3, S2*.

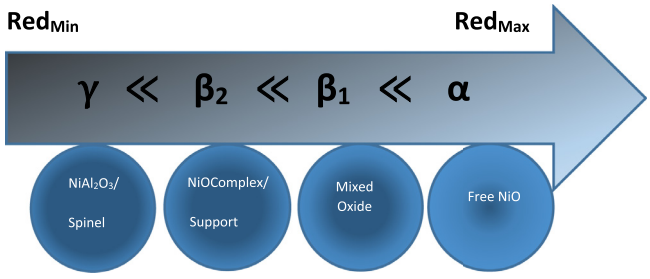

Fig. 4. Schematic representation of the TPR reduction bands for NiO/support interactions.

3.2.2. TPR analysis

The TPR analysis for all the catalysts studied is summarized in Fig. 3. Depending on the maximum positions, reduction of the NiO species can be classified into four different types: α, β_1, β_2 and γ [47,48]. The α type is related to nickel oxide species that have a weak interaction with the support, with a reduction temperature range of between 573 and 673 K (NiO-free species). The β_1 type is assigned to nickel oxide species (NiO plus Ni in a mixed oxide phase) that interact weakly or slightly with the support and are reduced between 673 and 873 K. The β_2 type corresponds to NiO species with a strong oxide/support interaction and is, therefore, less easy to reduce than the previous ones. In this case, there is a stable phase rich in Al with a reduction temperature of between 873 and 1023 K. Finally, the γ type (1023–1123 K) belongs to a much less reducible NiO in the nickel aluminate phase with a spinel structure [49,50]. In this latter case, the reduction temperature range is between 573 and 673 K. This classification is presented in Fig. 4 in decreasing order of reduction temperature.

A comparison between the TPR data for the synthesized catalysts is shown in Fig. 3a), and the maximum peak temperatures and fraction of the total area represented by each are included in Table 2. The deconvolution of overlapping peaks using a Gaussian fit for determination is shown in Fig. 3b). In the case of *S1*, the appearance of a single peak with a greater intensity than for the rest of the samples can be seen. This peak undergoes a complete reduction in the region of weak or poor NiO/support interactions, representing 99% of the total area of the peak. In this case, NiO is practically free as fine and/or amorphous particles, which favors self-sintering of the oxide and, therefore, grain growth of the active phase [48,51,52]. In contrast to *S1, S2* can be seen to contain four peaks. The first of these corresponds to a very small peak at the beginning of the region that can be attributed to a small fraction of widely dispersed nickel nanoparticles which interact weakly with the support and are easily reducible. The second appears at the upper limit of the α (weak interaction) and β_1 region (slight interaction), thus indicating an oxide fraction that interacts weakly with the support but more than that shown in *S1* [52]. In this case, both peaks represent 55.3% of the total reduction profile area attributable to the transitional regions α, β_1 and, therefore, the largest amount of reducible oxide obeys these kinetic characteristics. The third peak appears at the initial part of the β_1 region, thus indicating a slight Ni-Al interaction. This peak represents 37.4% and is due to mixed oxides as reducible species. The last peak for *S2* is found in the γ region, where the species were very difficult to reduce and where NiO interacts as Ni-Al_2O_4 (spinel-type material, 7.3%). The behavior of this sample can be represented as a weak interaction, with a small fraction of non-reducible species. Three peaks can be observed in the case of *S3*. The first appears at the lower limit of the β_1 region, in the range of 581 to 755 K, in other words it begins in the region of low interaction (α) and ends in the next region of slight interaction. This peak can be attributed to a weak NiO/support interaction and represents 45.1% of the total. The other two peaks are found in the β_1 (35.7%) and γ (19.2%) regions. In this case, a shift of the low interaction peak towards β_1 was observed, with an increase of approximately 11% in the fraction of poorly reducible species (γ) with respect to *S2*. Two peaks can be observed in the case of *S4*, one in the central part of the α region (62.5%) and the other in the β_1 region (37.5%), thus showing a mostly weak interaction followed by a stronger β_1-type interaction for mixed oxides.

In general, the catalysts mostly present weak interactions in all cases, and a possible relationship between the synthesis method, porosity and phase purity and the NiO interaction types with the support can therefore be considered. The most crystalline and purest sample (*S1*), which also exhibits the smallest porosity, presents a single type of interaction (weak) with a very well defined and high intensity peak. The maximum

Table 2
Maximum temperature and fraction of the peak areas of the TPR curves for the four NiO/La-HA catalysts.

Catalyst	Method	$T_{\alpha,m}$(K); Peak area fraction (%)							
		α		β_1		β_2		γ	
S4	RMAD	629	62.5	710	37.5	–	–	–	–
S3	MAD+PegMn	672	45.1	723	35.7	–	–	1093	19.2
S2	MAD	561;663	55.3	720	37.4	–	–	1036	7.3
S1	AD	622	99.9	–		–	–	–	–

is found very close to the reference value for the reduction of pure NiO particles ($T_{\alpha,m}$ = 673 K) [53] into large Ni^0 particles. In catalysts *S2* and *S3*, the displacement and appearance of new reduction peaks with respect to *S1* can be related to the presence of secondary phases that condition the interaction of NiO with the support. Although it is true that weak interactions continue to predominate, the secondary phases in both samples allow very similar profiles to be obtained. *S3* shows a decrease in the fraction of weak interactions with respect to *S2* and an increase in the presence of spinel-like Ni-Al_2O_4 species, which could be associated with a small increase in the percentage of the spinel structural phase with respect to *S2* and, therefore, *S1*. *S4* exhibits a behavior intermediate between *S1* and the other two catalysts as the largest peak (62.5%) occurs in the middle part of the weak interaction region ($T_{\alpha,m}$= 629 K). This behavior is very similar to that observed for *S1* but with an additional peak corresponding to a stronger interaction (mixed-oxide type) in the middle part of the β_1 region (37.5%). The Ni-spinel species is essentially absent. The reduction profile observed is more homogeneous than that observed for the other catalysts, which could be due to a phase of pure hexaaluminate.

3.2.2.1. Simulation analysis of TPR peaks for catalyst S1. In addition to providing qualitative information on the reduced species, reduction stages, reducible quantity, interaction with the support and the maximum peak temperature, the TPR analyses could also allow the reduction mechanism to be identified and the activation energy, kinetic rate of reaction and the parameters that determine its behavior to be determined. Another important aspect to mention is that the morphology in which the grains of the active phase grow during reduction could be predicted [54–56].

In order to better understand the predominant kinetic aspects of the catalysts, the reduction mechanism for *S1* was simulated as this sample has the highest crystallinity and the weakest metal-support interaction. To this end, TPR analyses were carried out by modifying the reduction heating rate: β (K/min) between 5 and 100, using a H_2/Ar mixture (5%, PRAXAIR) and a flow rate of 50 mL/min. The curves obtained from these TPR analyses at different β values are shown in Fig. 5a). A displacement of the maximum peak temperature (T_p) as the heating ramp increases, as well as the intensity of the maximum conversion obtained (α_p) at the corresponding T_p, can clearly be seen. The TPR results allow the behavior of the conversion over time $d\alpha/dt$ to be obtained by dividing the value obtained by the area of each peak. Fig. 5b) shows the normalized curves obtained by numerical integration of the TPR curves. The behavior of the conversion as a function of temperature for the various β values analysed, which correspond to the TPR peaks, can be seen. The methodology used has been included as Supporting Information.

The parameters obtained upon performing these simulations, at the several values of β, as well as the statistical parameters of fit, coefficient of determination (R^2) and the chi-squared parameter (χ^2), which predict the fit of the model to the experimental data, are summarized in Table S4. The kinetic parameters for all curves were calculated using the values provided in Table S4, giving: Ea = 61.5 kJ/mol and k_{ref} = 0.41 min^{-1}. A fit of better than 97.9% was achieved in all cases, along with very small values of χ^2, thus confirming that the simulations and the calculated results describe the reduction phenomenon studied for *S1*.

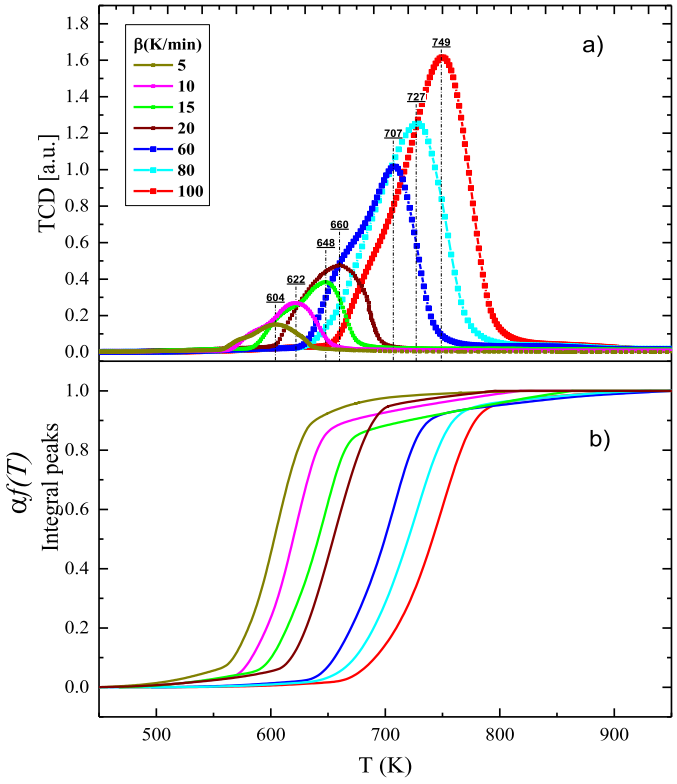

Fig. 5. a) TPR analysis curves obtained for various β values (K/min). b) Conversion as a function of temperature for the various TPR curves.

The *m* exponent, which according to the nucleation model describes the mechanism in which the oxide behaves during crystallization, gives an average value of 2.01, comprising the range between 1.89 for β = 5 K/min and 2.15 for β = 100 K/min. These results indicate that crystallization of the species formed upon interaction between nickel oxide/support and free NiO could occur two-dimensionally, morphologically speaking, producing large planar islands of a cluster type. Similarly, the low activation energy of the system coincides with the low metal-support interaction described previously (α-type), which favors the 2D growth of considerably sized clusters in which the reduction of oxides is practically complete.

Superposition of the experimental results and the simulations carried out using Eq. (S10), performing successive iterations until convergence with the results included in Table S4, are presented in Figure S1. The behavior and fit of the theoretical data with the experimental results are shown graphically, with a) showing the experimental TPR/Ap curves and b) conversion as a function of temperature. The residuals between the experimental values and the data obtained from the simulation can be seen in Figure S2. The most notable differences between the two curves are found in the tails of the TPR peaks as the model does not fully predict this behavior since they do not present a high randomness.

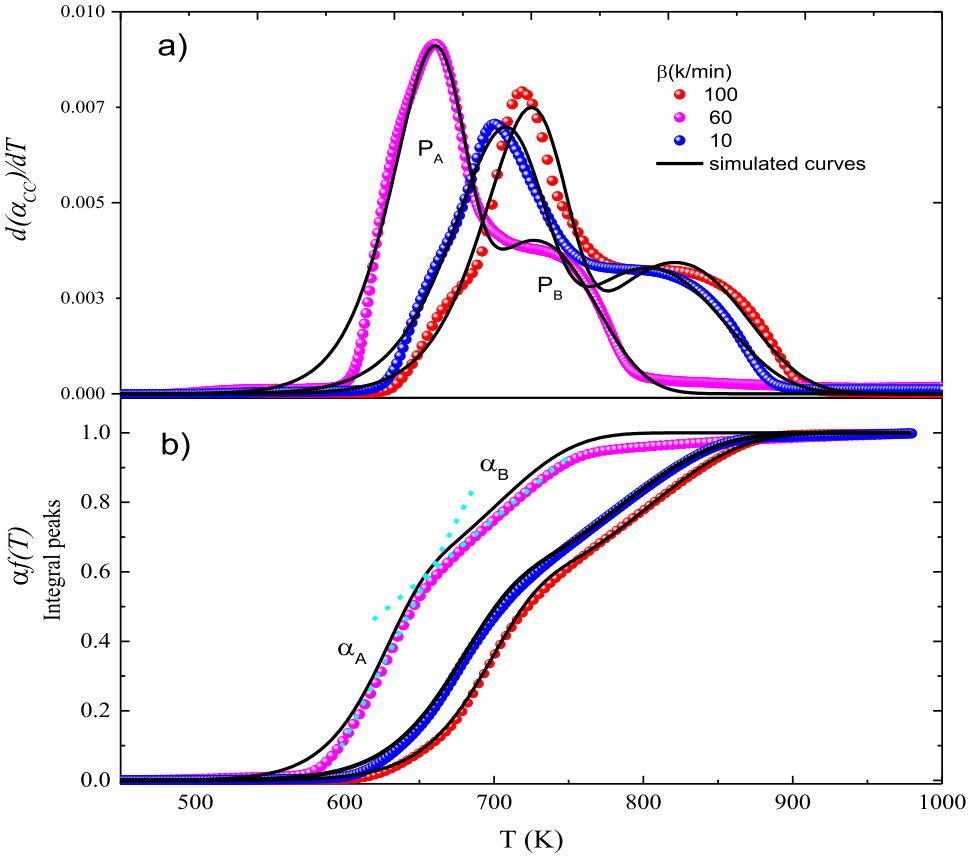

Fig. 6. a) Collapse of experimental TPR data and data from simulations carried out at various values of β for *S4*. b) Graphical comparison of the conversions obtained upon numerical integration of the experimental data and the simulations carried out.

This effect has a negligible impact on the fit of the results obtained (see Table S4).

The linearized form of the Kissinger equation shows a 98.28% fit with the experimental data, thus giving a value of E_a = 20.13 ± 1.07 kJ/mol and k_0 = 187.1 s^{-1}, which does not agree with the values obtained from the simulations (see Figure S3).

The results obtained using the Ozawa method are shown in Figure S3 ($E_a^* = 60.31 \pm 2.61\ kJ/mol$ and $k_{ref}^* == 3.75 * 10^{-3}\ s^{-1}$ (0.23 min^{-1}) for $m = 2.5$). The incorporation of the Ozawa exponent and the considerations included in the model give a very pronounced change of the slope for the data analyzed. These results allow a better fit and interpretation of the reduction phenomenon in which the activation energy values and rate constant k_{ref}^* are of the same order as the values obtained in the simulations (see Table S5). The two methods consider growth processes in terms of nucleation and temperature dependence, which gives more accurate information about what happens during the reduction reaction. The value of $m = 2.5; 2.01$ for Ozawa, and the simulations, suggest a two- or three-dimensional crystal growth for the nickel particles.

In the case of *S4*, where a multi-stage reduction occurs. The parameters obtained from the simulations using different β values, as well as the statistical parameters of fit, coefficient of determination (R^2) and the chi-squared parameter (χ^2), which predict the fit of the model to the experimental data, are summarized in Table S6.

The superposition of the experimental data and the curves obtained from the simulations with the different values of β can be seen in Fig. 6a). In all cases, the fits show an R^2 > 95% and very small values for χ^2 (see Table S6), thus suggesting that the model applied correctly predicts the reduction process for *S4*. The accumulated average activation energy gives the value $\overline{\mathbf{E_{a,CC}}}$ = 130 **KJ/mol**, with a value of $\overline{\mathbf{k_{ref,CC}}} = 3.03\mathbf{x}10^{-3}\mathbf{s}^{-1}$ (0.182 min^{-1}), thus confirming the greater interaction with the metal support described previously. The collapse between the simulated cumulative conversion curves and those obtained upon numerical integration of the experimental curves can be seen in Fig. 6b). For the various values of the heating ramp, the curve has two different slopes, which correspond to the functionalities α_A and α_B, respectively, up to the point of full conversion. A comparison between the experimental data and the simulated curves, as well as the residuals of the model fit for the β values analyzed, can be found in Figure S4 a). The deconvolution of the peaks P_A and P_B, which together make up the accumulated curve, is also shown (dashed lines). Two peaks can be seen in all cases, with P_A always presenting a larger area than P_B (see Table S6). In contrast, the values of the activation energy are $P_B > P_A$, where $\overline{E_B} = 70.0\frac{KJ}{mol}$ and $\overline{E_A} = 60.96\frac{KJ}{mol}$, which could mean that slightly larger fraction of species has a low interaction and the rest a higher interaction. In the case of *m*, this study shows that $\overline{m_A} = 1.83$ and $\overline{m_B} = 1.13$, which could indicate, in the case of P_A, that the particles are growing in one or two dimensions following the Avrami nucleation model, whereas for P_B this value of *m* could indicate a random nucleation with unimolecular decay. The residuals between the model and the experimental data are also shown in Figure S4 b), which shows that the range of variability is between $\pm 8 \bullet 10^{-3}$. These values are very well distributed in the variability zone, thus corroborating the fits found.

3.2.3. Morphological study by SEM analysis

In an attempt to better understand the catalytic performance of the catalysts, the morphologies of *S1* and *S4* after calcination were analysed. The SEM images presented in Figs. 7 and 8 show the morphologies and grain/particle distributions for both catalysts. Fig. 7 shows the SEM images and distribution of NiO areas for *S1* after calcination, with NiO/support clusters being perfectly visible on the catalyst surface. Flat islands of oxide can also be seen on the hexaaluminate microstructure, with the areas of these being large compared with the scattered particles (Fig. 7g)). As such, it can be assumed that the largest mass fraction of NiO has this morphology (islands with an average area of 69.16 μm^2), with a small fraction being present as more dispersed particles (area

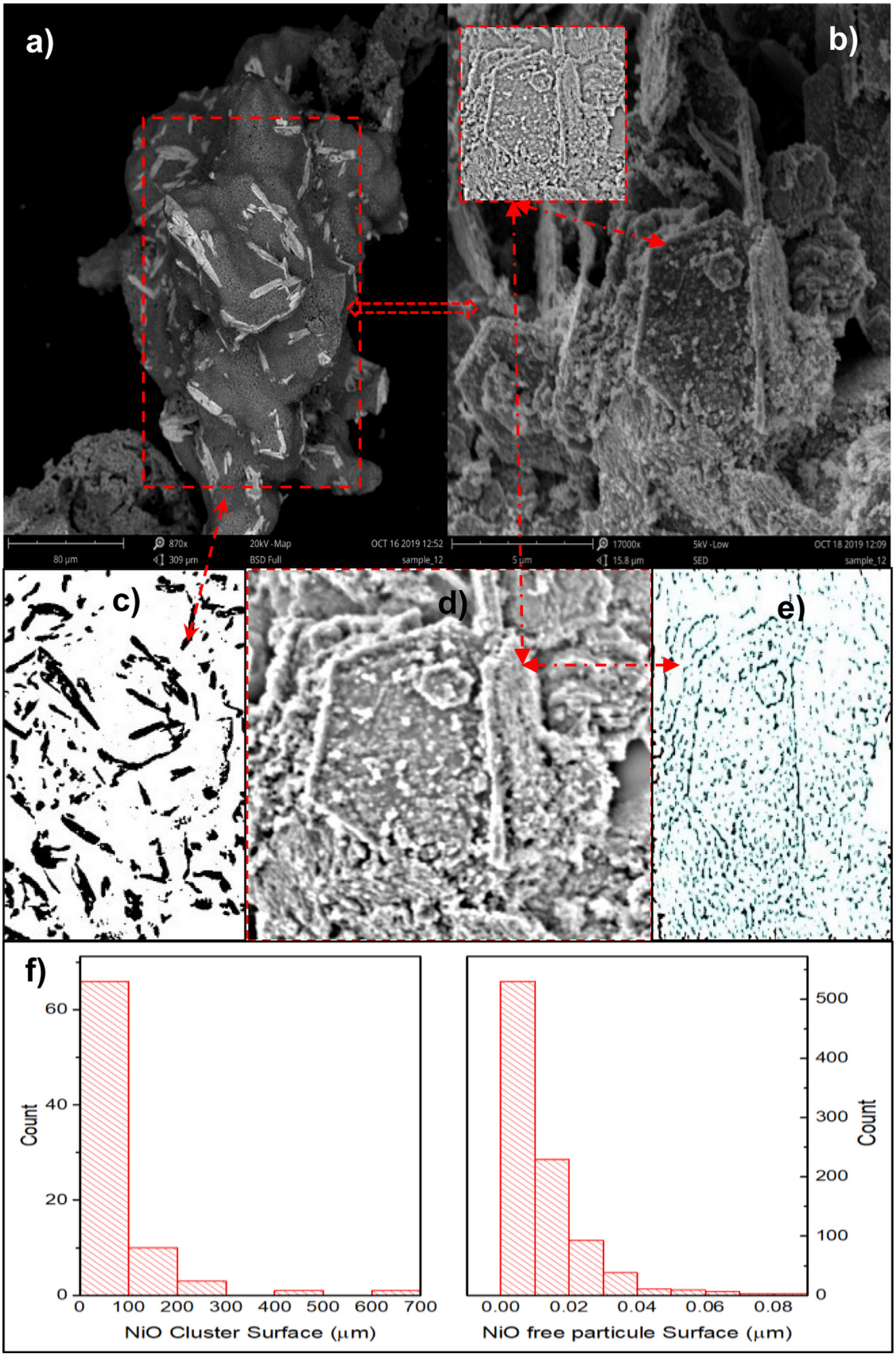

Fig. 7. SEM-EDX images for *S1* after calcination at 673 K. a) SEM cluster 2D image of NiO species in 10% Ni/LaHA. b) Microstructure and NiO particles dispersed in 10% Ni/LaHA. c) Image of isolated clusters in a) using low-pass filters. d) Application and filtering of the box in b) to identify nickel particles dispersed on the hexaaluminate microstructure. e) Segmentation of the particles on the hexaaluminate microstructure to determine areas. f) Area distribution for clusters and free NiO particles.

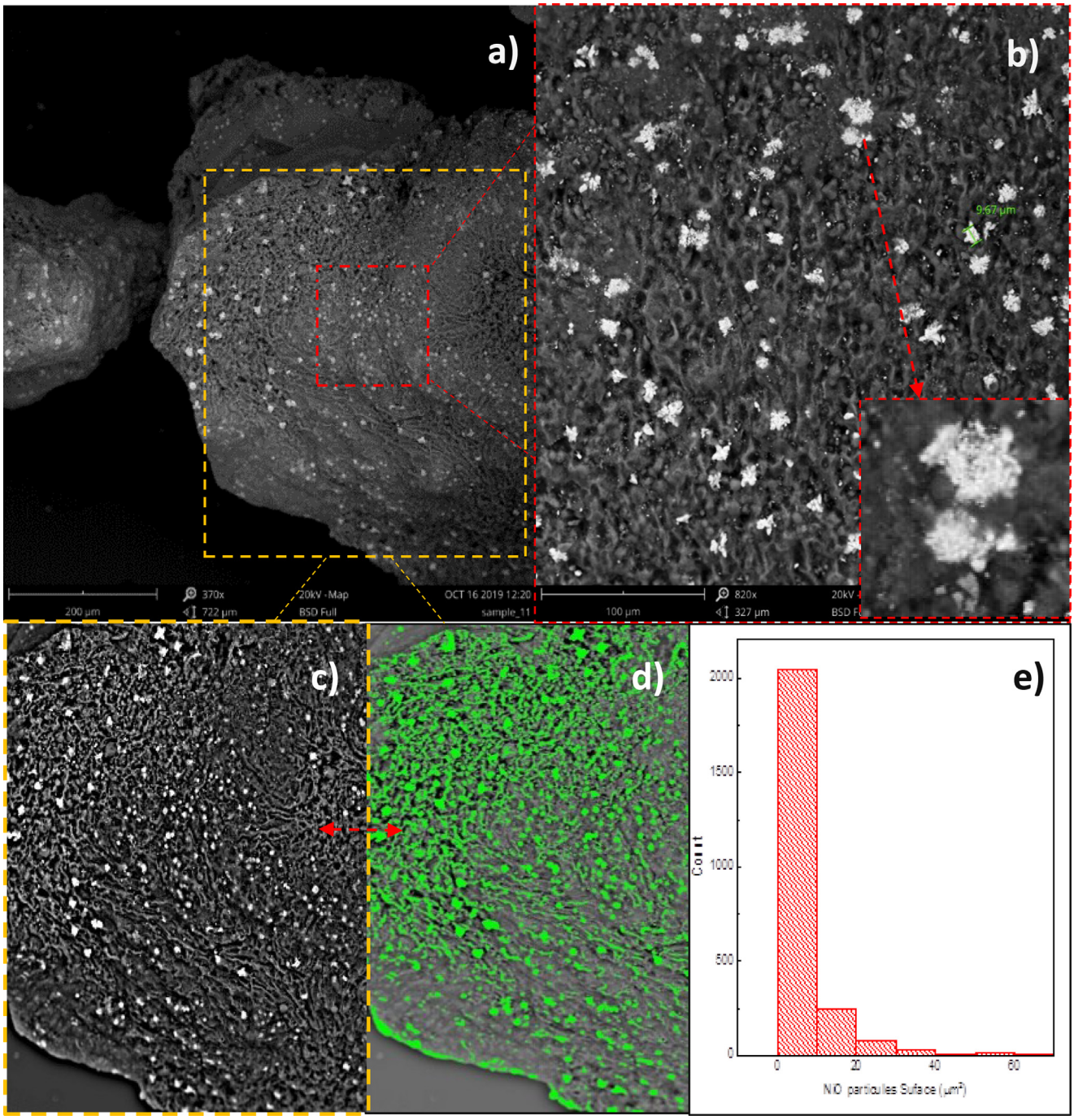

Fig. 8. SEM images and distribution of grain areas for *S4* after calcination at 673 K. a)-b) SEM images and magnification of surface grains of NiO in 10% Ni/LaHA. c) Microstructure and NiO particles dispersed in 10% Ni/LaHA. c) d) Image analysis for identification of NiO grains in 10% NiO/LaHA. e) Distribution of the grain area in images c) d).

of 0.012 μm^2) on the surface of the hexaaluminate microstructure. The SEM images of catalyst *S4* are shown in Fig. 8, which clearly shows a marked morphological change in terms of the NiO grains and their distribution with respect to *S1* (see Fig. 7). Thus, the particle clusters present interstices that could facilitate close contact between the oxide (see box Fig. 8b)) and H_2 during reduction, and gasses during the reaction. Another easily distinguishable aspect is that a better distribution of the oxides on the surface of the catalyst is observed in *S4* (see Fig. 8c) d)), with the presence of particles with a smaller area compared to *S1* (average of 6.7 μm^2 for those closest to the surface). As such, smaller particles with lower masses are found, thus inferring that there are a large number of very small particles on the microstructure of the catalyst, thus possibly improving its reaction performance compared to the other catalysts. This type of morphology and metallic dispersion could be responsible for generating β_1 interactions with the support in *S4* and, together with the porosity achieved, contributing to a better behavior in terms of stability and conversions during DRM [57–59].

The SEM images for *S4* [a), b), c)] and *S1* [d), e), f)] after reduction are shown in Fig. 9. The appearance of plateau-type reliefs, which create wells containing the hexaaluminates and the secondary phases (γ-alumina/spinel), along with the presence of porosity, is also noticeable. Fig. 9b), c) shows Ni^0 grains with a quasi-spherical morphology on

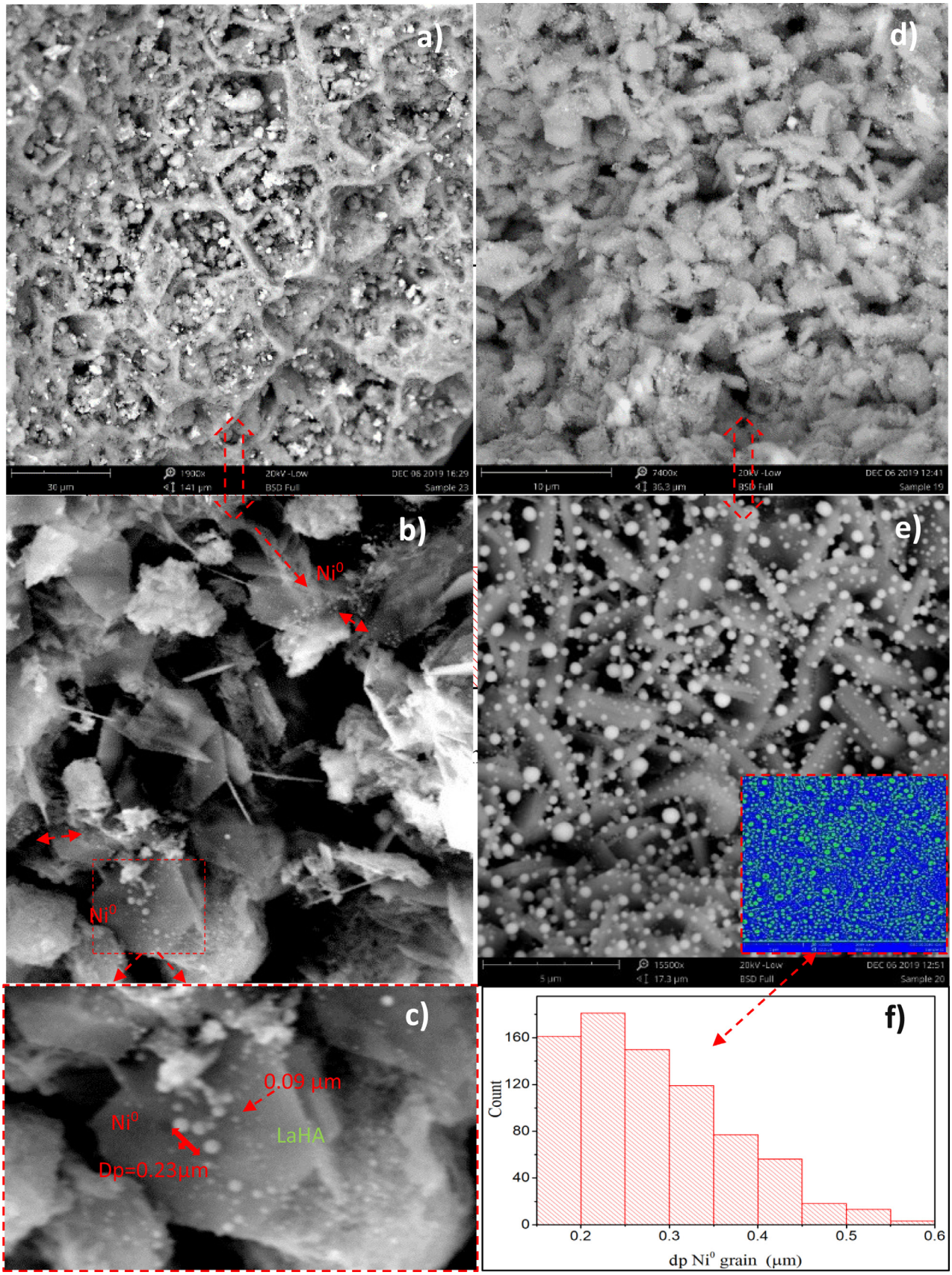

Fig. 9. SEM images for catalyst *S4* [a), b), c)] and *S1* [d), e)] after reduction with H_2. f) Garno size distribution for *S1* 10% NiO/LaHA.

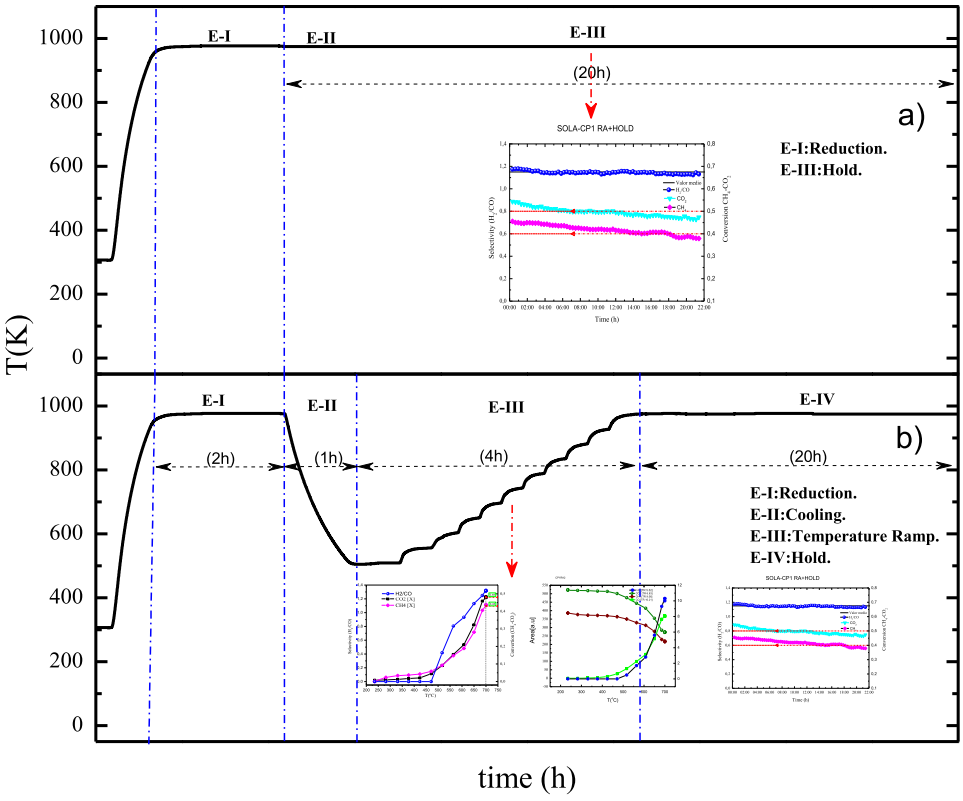

Fig. 10. Initial reaction procedures used in evaluation of the catalytic performance for the catalysts. a) Stability test at 973 K for 20 h. b) Catalytic performance at various temperatures followed by catalytic stability.

the surface of the hexaaluminates, these grains having a maximum size of 0.23 μm for the small fraction that can be observed. The remaining grains have a size of between 0.04 and 0.09 μm. The values are very different from those observed for *S1* in Figs. 9e), f), for which the grain size distribution was calculated and the average diameter of which is 0.28 μm. The size distribution covers sizes above 0.4 μm in the region analysed. These values differ markedly from those observed for *S4*, for which sizes lower than 0.09 μm were not observed. In light of these results, and as indicated previously, *S4* appears to present a better dispersion and distribution of nickel particles in this support with respect to *S1*. As such, it can be inferred that *S3* and *S2* also replicate this morphological and distributive behavior of the active phase in the support, a result that should also be evidenced in the catalytic performance of these catalysts in DRM [57–59].

3.3. Catalytic performance

The initial reaction procedures to which the catalysts were subjected are summarized in Fig. 10. Fig. 10a) shows the catalytic stability of the samples after reduction with H_2 for 2 h followed by reaction at 973 K for 20 h. Fig. 10b) shows the catalytic performance at several temperatures for 4 h, preceded by the reduction and cooling stages (2 and 1 h, respectively) and, finally, an isothermal stage at 973 K for 20 h.

Reactant conversion $[X]_i$, selectivity $[H_2/CO]$, carbon balance (CB), and product yields ($Y_{CO}Y_{H_2}$) were calculated using the following equations:

$$[X]_{CH_4} = \frac{[CH_4]_{in} - [CH_4]_{out}}{[CH_4]_{in}} \tag{8}$$

$$[X]_{CO_2} = \frac{[CO_2]_{in} - [CO_2]_{out}}{[CO_2]_{in}} \tag{9}$$

$$Y_{H_2} = \frac{[H_2]_{out}}{2*[CH_4]_{in}} \tag{10}$$

$$Y_{CO} = \frac{[CO]_{out}}{[CH_4]_{in} + [CO_2]_{in}} \tag{11}$$

$$\text{Selectivity}\left[\frac{H_2}{CO}\right] = \frac{Y_{H_2}}{Y_{CO}} \tag{12}$$

$$CB = \frac{[CO_2]_{out} + [CO]_{out} + [CH_4]_{out}}{[CH_4]_{in} + [CO_2]_{in}} \tag{13}$$

The stability of the catalysts in the reaction was tested by performing long catalytic runs (20 h). The evolution of CH_4 and CO_2 conversion with time-on-stream is presented in Fig. 11 for all four catalysts. *S4* was found to be more stable throughout the reaction stage, with an average H_2/CO selectivity of 1, followed by *S3*, with an average selectivity of 0.99 over the first 14 h, subsequently decreasing to 0.82. *S2* shows a very similar behavior to *S3* but with an average value of 0.95 over the first 14 h, subsequently decreasing to 0.85 at the end of the test. This abrupt change in slope is due to the increase in the amount of CO produced, which can be attributed to the RWGS reaction [1,7], and a decrease in the amount of H_2 at the reactor outlet. *S1* presented a much lower initial selectivity, with a practically constant negative slope and decreasing selectivity over the period of time analyzed, along with an initial H_2/CO selectivity of 0.9 and final value of 0.73.

The conversions for CO_2 and CH_4 are shown in Fig. 11b) and c), from which it can also be seen that *S4* exhibits the highest conversion in both cases. *S4* shows the lowest degree of deactivation with respect to the other samples ($\Delta\alpha_{CO_2} \approx 4\%$ and $\Delta\alpha_{CH_4} \approx 10\%$), which after 20 h gave essentially equal coverage values that were much lower than those for *S4* ($\alpha_{F-CO_2} \approx 55\%$; $\alpha_{F-CH_4} \approx 40\%$). It can be assumed that there is a direct correlation between the selectivity and S_{BET} for all catalysts, since *S4* shows the highest stability/selectivity and *S1* gives the lowest values. It is well known that DRM cannot occur spontaneously below 915 K, and that the secondary reactions (methane decomposition and Boudouard reaction) take place at a significant rate between 910 and 973 K. As such, it is necessary to use a reaction temperature higher than 1023 K to minimize the effect of these side reactions and catalyst deactivation

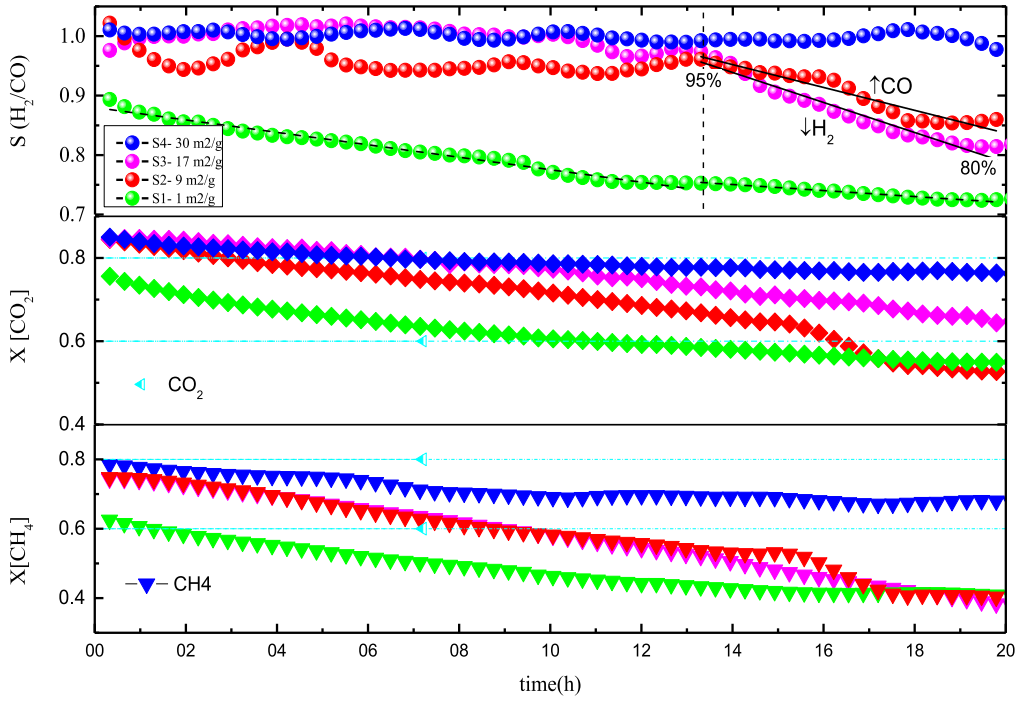

Fig. 11. Stability of the catalysts at 973 k for 20 h. a) H_2/CO selectivity. b) CO_2 conversion. c) CH_4 conversion.

[60–63]. Another reaction that affects DRM is the well-known RWGS, which results in an H_2/CO value lower than 1, although this reaction can be completely inhibited above 1090 K. The Boudouard reaction is also inhibited at high temperatures, at high temperatures the Boudouard reaction is inhibited but the reaction of cracking of methane is increased, main reason for the deactivation of the catalyst by deposition of coke [1,7,11,64].

The carbon balance for the catalysts, as calculated using Eq. (13), is shown in Figure S5. It can be seen that this balance affects deactivation of the catalyst, with a maximum of approximately 82% carbon after reaction for 20 h for the first three catalysts. Although the initial value for *S1* is higher than for *S2* and *S3*, these values converge by the end of the reaction. In contrast, *S4* starts with a value similar to *S2* and *S3* but increases by only 5% by the end of the reaction period. Although the first three catalysts have higher deactivation values compared to *S4*, they still remain active and are not completely deactivated. It may be the case that the porosity generates a positive effect against catalyst deactivation, with greater porosity leading to greater activity and less deactivation.

To try to elucidate the dynamic behavior of the catalyst, the yields of H_2/CO, as calculated using Eqs. (10) and (11), are shown in Fig. 12. *S4* exhibits the most stable behavior and most uniform performance, with the CO yield decreasing by only around 6%. In contrast, the other catalysts presented differences of approximately 20% for *S3/S2* and 11% for *S1*. In the case of H_2, the yields were generally lower than those for CO for all catalysts here we can also see a sudden change in the slope of the yield curve whose decreasing magnitude is greater than that of CO for its respective sample. This behavior could indicate that H_2 production is affected in the reaction, either due to consumption of this gas together with another reactant/product or to the effect of competition in the conversion of CH_4 with another secondary species generated in the reactor, thus resulting in coking of the active site. The pronounced separation between the H_2–CO performance curves for all catalysts allows us to qualitatively identify in which of them DRM predominates over time and from which range this predominance decreases.

The volumetric fractions for the different gasses (CH_4, CO_2, H_2, CO) at the reactor outlet are shown in Figure S6. It can be seen from this figure that the fractions of these gasses at the outlet vary markedly as the porosity of the catalysts decreases. The approximate rates of change of the volume fraction are shown in Table S7. *S4* (Figure S6 a)) exhibits the best stability in terms of both H_2 and CO production, and in the conversion of CO_2 and CH_4. This catalyst shows the lowest rate of change (Δc) with respect to the other three catalysts. Thus, arguably, although there is a small decrease in catalytic activity due to coke formation, this decrease is not sufficient to prevent the main reaction (DRM) from being sustained throughout the catalytic study. In contrast, the behavior observed for *S3* (see Figure S6 b)) changes radically. In the case of this catalyst, it can be seen that the H_2 production rate decreases with a steep slope (−0.069) from the start of the reaction. This evolution is very similar to that for catalysts *S1* and *S2* (see Table S7), and much higher than that expected for *S4*, even though they all have very similar initial values. In the case of CO, the highest rate of change was found for catalyst *S3* (−0.042), slightly higher than that obtained for catalyst *S2* (−0.045). From these results, it could be seen that secondary reactions begin to have a more notable effect in terms of catalyst coking, thus increasing deactivation. Although these reactions do not completely deactivate the catalyst, they nevertheless influence the CO and H_2 yields. The species can be ordered in descending order of approximate absolute exchange rate ($|\Delta c|$) as follows: $\Delta c^{H_2} \gg \Delta c^{CH_4} \gg \Delta c^{CO} \gg \Delta c^{CO_2}$. For complete conversion, this would have to be zero or, in the case of thermodynamic equilibrium, $\Delta c^{CH_4} \cong \Delta c^{H_2}$ and $\Delta c^{CO_2} \cong \frac{\Delta c^{CO}}{2}$, with this behavior being observed for *S1* (Figure S6 a)). A thermodynamic behavior similar to *S3*, where the performance of H_2 and CO decreased much faster than the conversion of CH_4 and CO_2, respectively, was also observed for *S2* and *S1*. Analysis of the Δc residues (see Table S7) corroborates the above, with *S4* having residues closest to zero, followed by *S2, S3* and *S1*. Negative magnitudes may be indicative of simultaneous reactions competing for products and reagents. In the case of *S3*, it can be seen that $\Delta c^{CH_4} \gg \Delta c^{CO_2}$ (2.7-fold), thus meaning that in the global equilibrium, the system favors the reaction of CO_2 with other species, and to a lesser extent the reaction with CH_4. Similarly, the negative residual value (R1, Eq (14)) between the slopes in *S3*, with a value of −0.009, indicates that the more marked downward behavior in the performance of H_2 is responsible for both the low conversion of CH_4 and

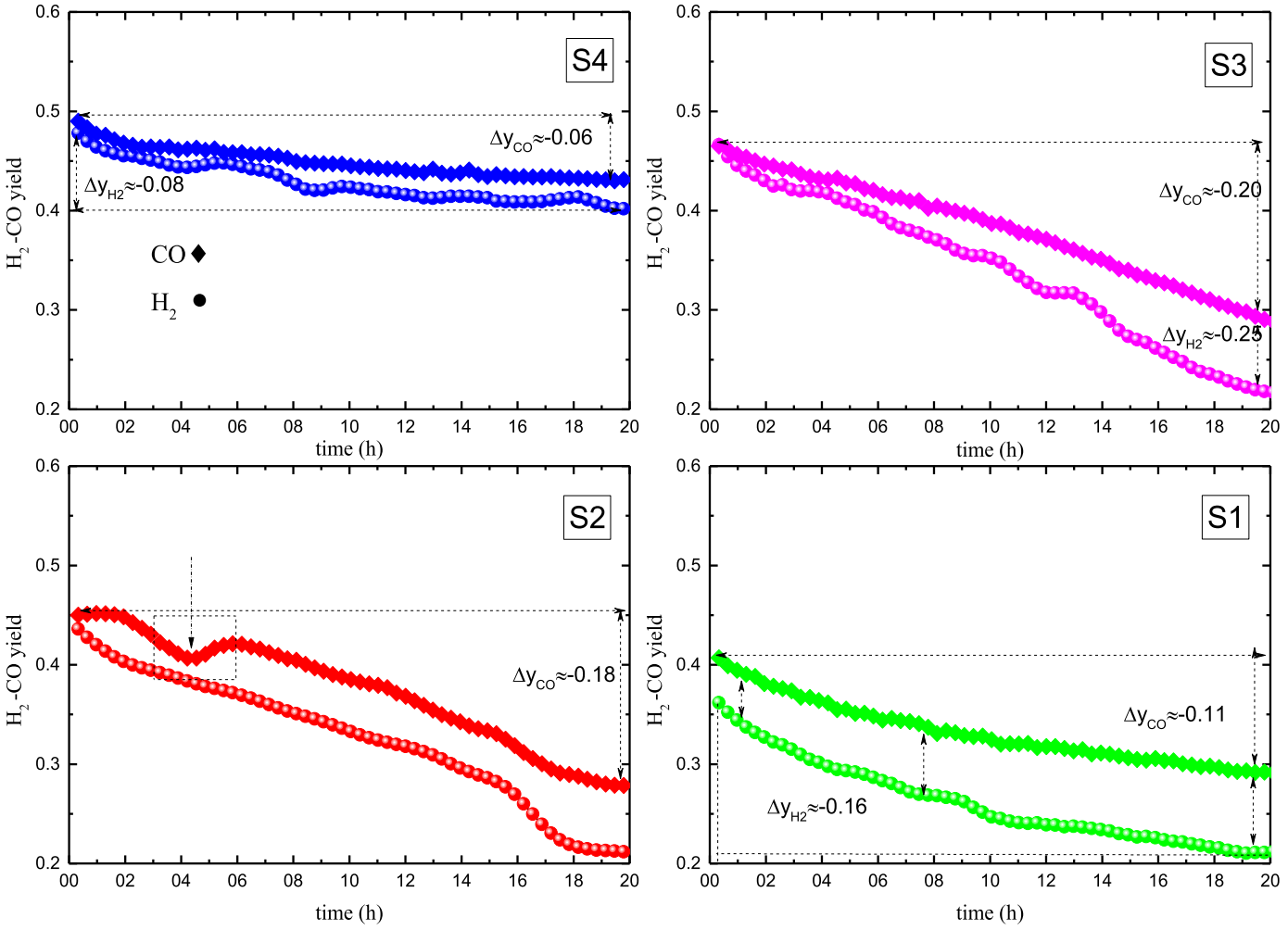

Fig. 12. Yields of H_2 (diamonds) and CO (balls) after reaction for 20 h.

its consumption in another parallel reaction. In the case of the residuals of the slopes for CO (R2, Eq (15)), it can be seen that these values are smaller and tend to zero, following the conversion values much more in the case of H_2. As such, simultaneous competition reactions appear to affect H_2 performance more directly than CO as a consequence of a non-selective consumption of methane with respect to CO_2.

$$R1 = \Delta c^{CH_4} - \Delta c^{H_2} \tag{14}$$

$$R2 = \left(\frac{\Delta c^{CH_4} + \Delta c^{H_2}}{2}\right) - \Delta c^{CO} \tag{15}$$

As can be seen from the scheme in Fig. 10b), the catalytic performance was also studied at various temperatures (Fig. S7), with significant differences being found between the catalysts. Thus, *S4* exhibits higher selectivity values than *S1*, which starts at a much lower temperature (750 K) than *S1* (840 K). The final selectivities (0.8 for *S4* and 0.63 for *S1*) could indicate that the RWGS reaction is favored at low temperatures, with the effect of this reaction decreasing upon increasing the temperature up to 973 K, where DRM begins to dominate the system. It should be noted that CO and H_2O production by the RWGS reaction, and subsequent coking due to possible CO decomposition, were not totally deactivated, although only a small fraction appears to be affected. The CO_2–CH_4 conversions and CO–H_2 yields also show that *S4* performs better at lower temperatures than *S1*, with methane conversion being more marked than CO_2 up to 790 K. Above this temperature, the CO_2 conversions exceed those of CH_4 until the final temperature, with conversions reaching 0.48 and 0.43 for CO_2 and CH_4, respectively, with *S4*. In the case of *S1*, CH_4 conversion is greater than that of CO_2 over the entire temperature range studied, exhibiting a greater separation at 700 K, with final values of 0.44 and 0.33, respectively. It therefore appears that, although the increase in temperature improves the conditions for the DRM reaction, it does not disrupt the initial dynamics, which are maintained throughout the temperature range, giving lower conversion values for *S4* and more distant between them, if the conversions obtained with *S1* are compared.. In the case of CO and H_2 yields, *S4* produced a greater quantity of CO, starting at lower temperatures than *S1* and remaining unchanged throughout the temperature range. As for H_2 yield, its production at the reactor outlet is displaced up to 700 K, but perhaps its generation not, since if we see the high conversion values of methane and CO production, in *S4*, we can see that they originate at similar temperatures, thus promoting CH_4 decomposition (Eq. (2)) and steam reforming reactions (Eq. (7)). This behavior would increase CH_4 consumption, possibly as a result of reacting with H_2O(g) produced by the RWGS reaction (Eq. (3)), and hydrogenation of CO_2 and CO (Eqs. (5) - (6)), which also consume H_2 and produce coke, and whose domains would be interrupted with the increase in temperature, as mentioned above. In the case of *S1*, H_2 production can be seen at the reactor outlet from 800 K, although CO is seen from approximately 630 K, very close to the temperature at which the greatest separation between the conversions of CO_2 and CH_4 occurs. These results could indicate that, before reaching 700 K, there is a simultaneous competi-

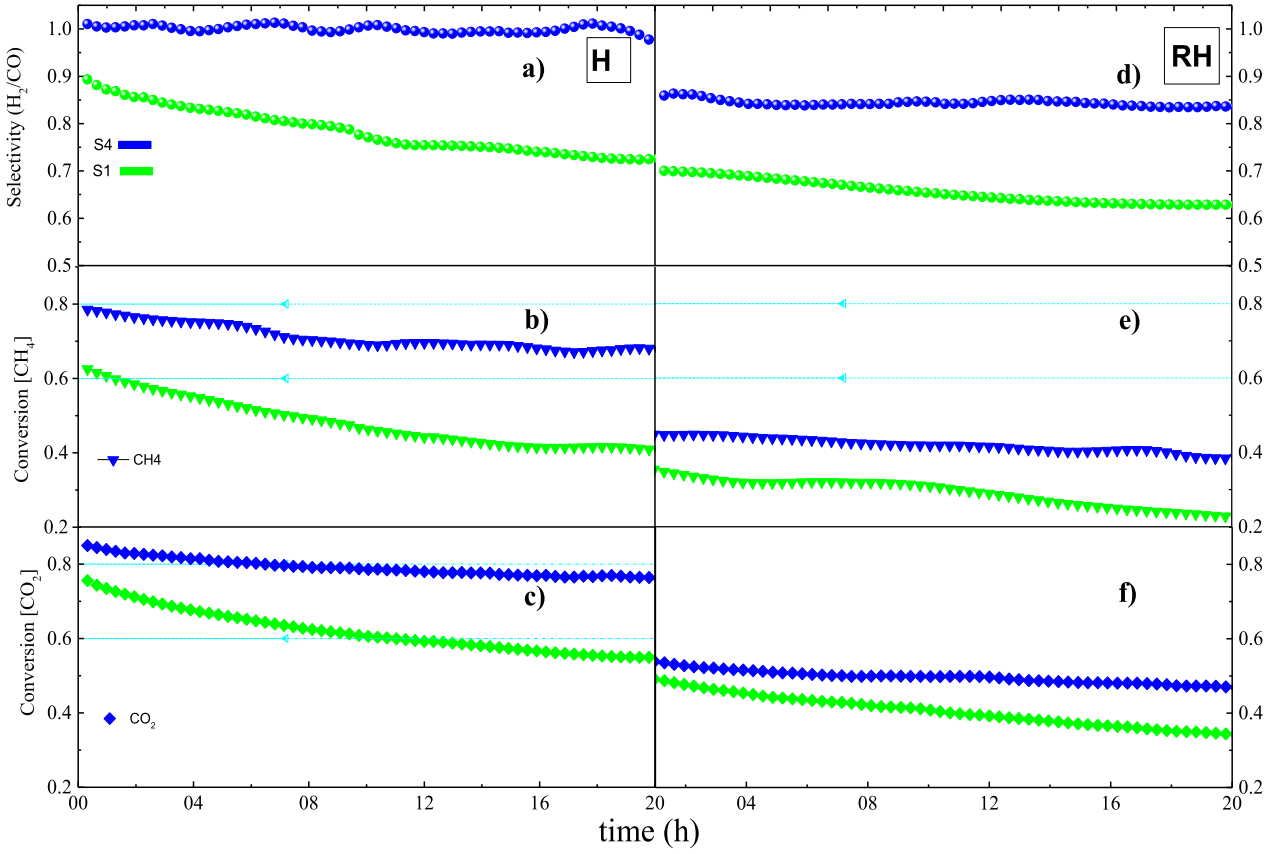

Fig. 13. Comparison between catalytic stability and conversions with the two reaction schemes (see Fig. 10) for *S4* and *S1*. a), b), c) correspond to selectivity, CH_4 and CO_2 conversion, respectively, for *S4* (blue) and *S1* (green) at 973 K after reduction for 20 h (see Fig. 10a)). d) e) f) same as a), b), c) but applying a kinetic ramp, followed by reaction at 973 K for 20 h (see Fig. 10b)).

tion between DRM (Eq. (1)), RWGS (Eq. (3)) and CO_2 hydrogenation (Eq. (5)) since these processes result in a high consumption of CO_2. Any H_2 produced would be consumed by the reactions in Eqs. (3)–(5), thus possibly explaining why CO is produced at lower temperatures and not H_2, as well as the greater conversion of CO_2 to CH_4 and deactivation due to coke deposition as a result of CO_2 hydrogenation. The carbon balance for both catalysts is shown in Figure S7 c), with maximum values occurring at low temperatures and decreasing as the temperature increases for both samples. It should be noted that *S1* has higher values of this indicator, (CB), compared to *S4*, thus showing greater inactivation and whose behavior is consistent with the parameters previously analyzed.

The results found for *S4* and *S1* upon applying and comparing the reactions strategy included in Fig. 10 are presented in Fig. 13. In the case of the H_2/CO selectivity obtained for both schemes, it can be seen that the heating ramp applied during the reaction negatively affects the performance of the catalyst, which leads to a selectivity well below (0.85) the average value found when the procedure included in Fig. 10a) was applied. The process for evaluating the reaction with a differential temperature increase appears to favor the appearance of secondary reactions that generate coke, thus reducing the performance even when an operating temperature range that favors DRM is reached. CO production is even higher than H_2 at the reactor outlet, which could be the result of an RWGS reaction as the main mechanism.

The conversions of CO_2 and CH_4 by *S4* show the same behavior as the H_2/CO selectivity. For *S1*, the values for both processes differ from those shown by *S4*, with both H_2/CO selectivity and CH_4 and CO_2 conversion maintaining a constantly decreasing behavior with practically equal slopes. It appears that both strategies are connected in time because the values of the curves are intertwined and seem to be continuous with each other. It also appears that, in both cases, the system is governed by the same reaction dynamics and the competition between equilibrium reactions remains almost the same.

3.3.1. TEM analysis of catalysts after catalytic tests

HR-TEM/EDS images for *S1* and *S4* recorded after the DRM reaction are shown in Figs. 14 and 15. Fig. 14(a) (b) (c) (d) clearly shows a hexaaluminate microstructure on which large Ni^0 grains (about 200–250 nm) are visible, along with other smaller grains (20–30 nm) that show low or no interaction with the support, as observed in the TPR analysis. The effect of this low support-metal interaction is that the nickel particles can migrate easily on the surface of LaHA, where they encounter other particles and increase in size by a diffusive effect. The grains were found to be essentially fully covered with coke, thus resulting in deactivation of the metal sites. Another notable aspect was the formation of large circular aggregates (see Fig. 14e) f) g)) of graphitic carbon surrounding the nickel grains. The Ni^0 nanoparticles were distributed around the graphitic area, as can be seen in Fig. 14h). The mapping of the elemental composition of the species, as well as the presence of carbon in the form of graphite over the entire structure, can be seen in Fig. 14j) m). It can be seen how this carbon uses nickel to grow in a circular way around it, thus blocking the active metal sites, after which the Ni^0 is distributed to form a large cluster (see Fig. 14k)). The other elements that make up the structure are present in almost imperceptible quantities, thus confirming the independence of the metal and the support and explaining the low interaction, the growth of large Ni° cluster and facilitating carbon deposition and growth around Ni^0.

The morphology of the Ni^0 grains and nanoparticles on the support, as well as their distribution, can be seen in Fig. 15(a) (d) (*S4*). The grain

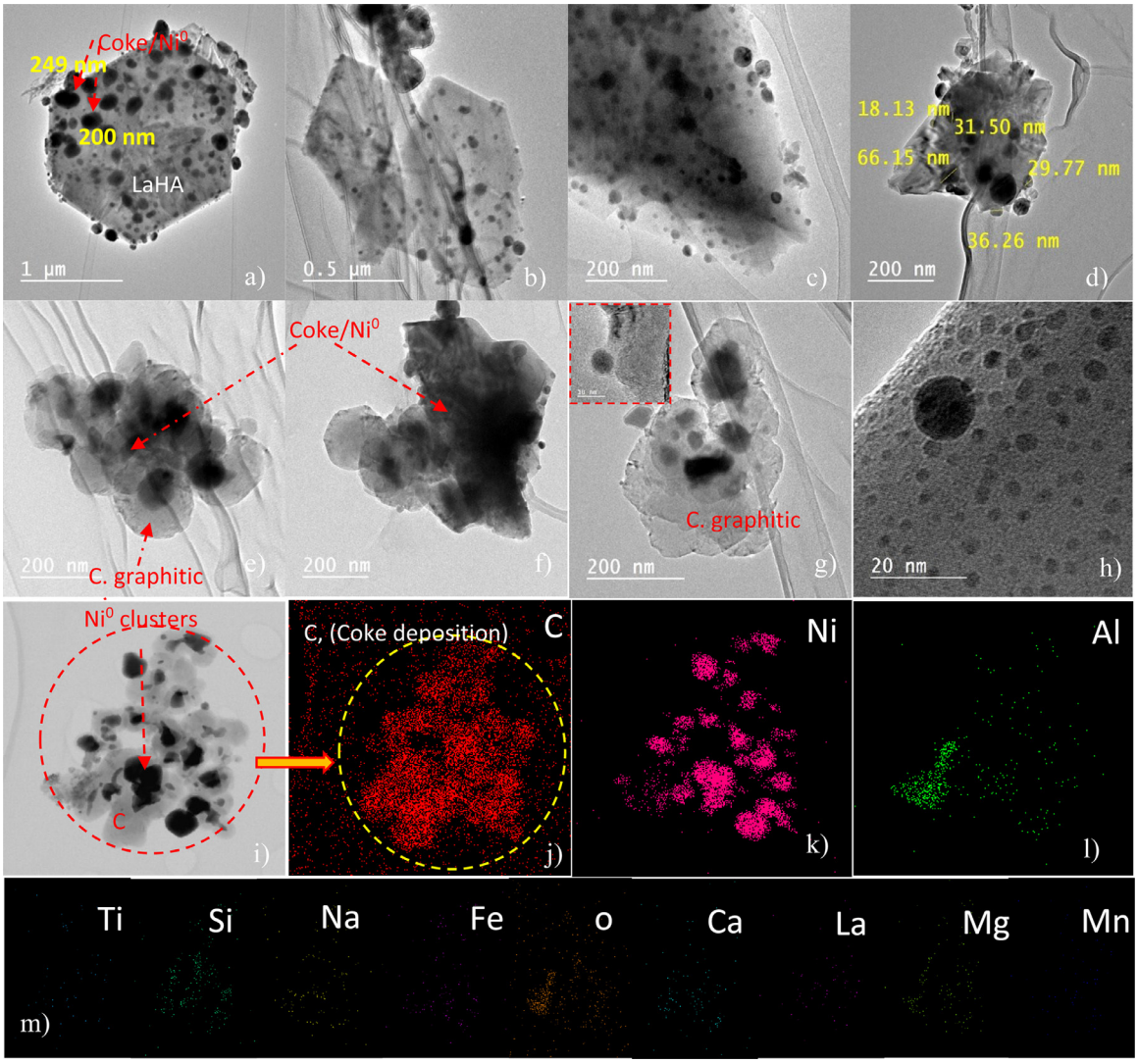

Fig. 14. TEM images and EDS mapping for *S1* after DRM for 20 h. Metallic nickel grains on the hexaaluminate microstructure [a), b), c), d)]. Nickel cluster with coke deposits [e) f) g) h)]. TEM-EDS mapping for nickel cluster [i), j), k), l), m)].

size was uniformly distributed over the entire surface of the support, with an average size of 18 nm. As in the case of *S1* (Fig. 14), an intimate contact was found between the metal phase and the support for *S4*. This contact exerts a fixing effect on the nickel particles, thus preventing an increase in kinetic energy from causing surface diffusion and increasing the size of the grains. The presence of nickel particles distributed on the surface of the support, and the coke deposits that grow in various forms around them, can also be seen in this figure. Nanotubes and layered carbon were also detected (see Fig. 15(h)). Fig. 15(j) (m) shows a high dispersion of nickel particles compared to *S1* (Fig. 14k)), with these particles being evenly distributed on the support. This high dispersion could be related to the better performance of *S4* than *S1*. It is known that the presence of promoters like La improves the resistance to coke deposition [15,64] as a result of an interaction with the metallic phase, as can seen in Fig. 15m), where La is present between the nickel particles, (although it is worth mentioning that it is competing with other cations such as Na, Ca, K involved in the inactivation of the catalysts and that they are present by leaching during the extraction of acid solution, which could be reducing the efficiency of La^{3+}). A comparison of the mapping of *S4* and *S1* and the TPR analysis shows that the nickel particles in *S4* interact more strongly than in *S1* [53]. In the case of *S4*, the Ni^0 interaction with the support is much stronger, thus meaning that the metallic particles are unable to migrate easily on the surface and increase in size. It was also observed that the types of coke deposit have much less effect, in terms of blocking the active sites, in *S4* than in *S1*, thus resulting in better stability and greater resistance to deactivation. In light of the above, *S2* and *S3* are expected to behave similarly with each other, with a behavior intermediate between the two previous catalysts.

The HR-TEM images for *S2* [a), b), c)] and *S3* [d), e), f)] are shown in Fig. 16. The average grain size in *S2* is 11.94 nm (16.0 nm for *S3*). With regard to the carbon deposition, it was possible to identify graphite carbon in the case of *S2*, similar to the coke deposited in *S1*, and layer filaments for *S3*, which exhibits coke deposition very similar to *S4*. The deposition at active sites was much greater than in *S4*, in which the density of active sites due to the effect of porosity is lower. The order of the catalysts in relation to their porosity, activity and less carbon deposition is therefore *S4* >> *S3* >> *S2* >> *S1*. The hexagonal network pattern of the hexaaluminate phase for *S2* and *S3* can clearly be observed (see Fig. 16a), d)), and the rings and distances in the network of the polycrystalline phases of which they comprise can also be identified (see Fig. 16b), c), e), f)).

The values for the interlinear distances, as determined from analysis of the TEM-SAED images, as well as the identification of the possible

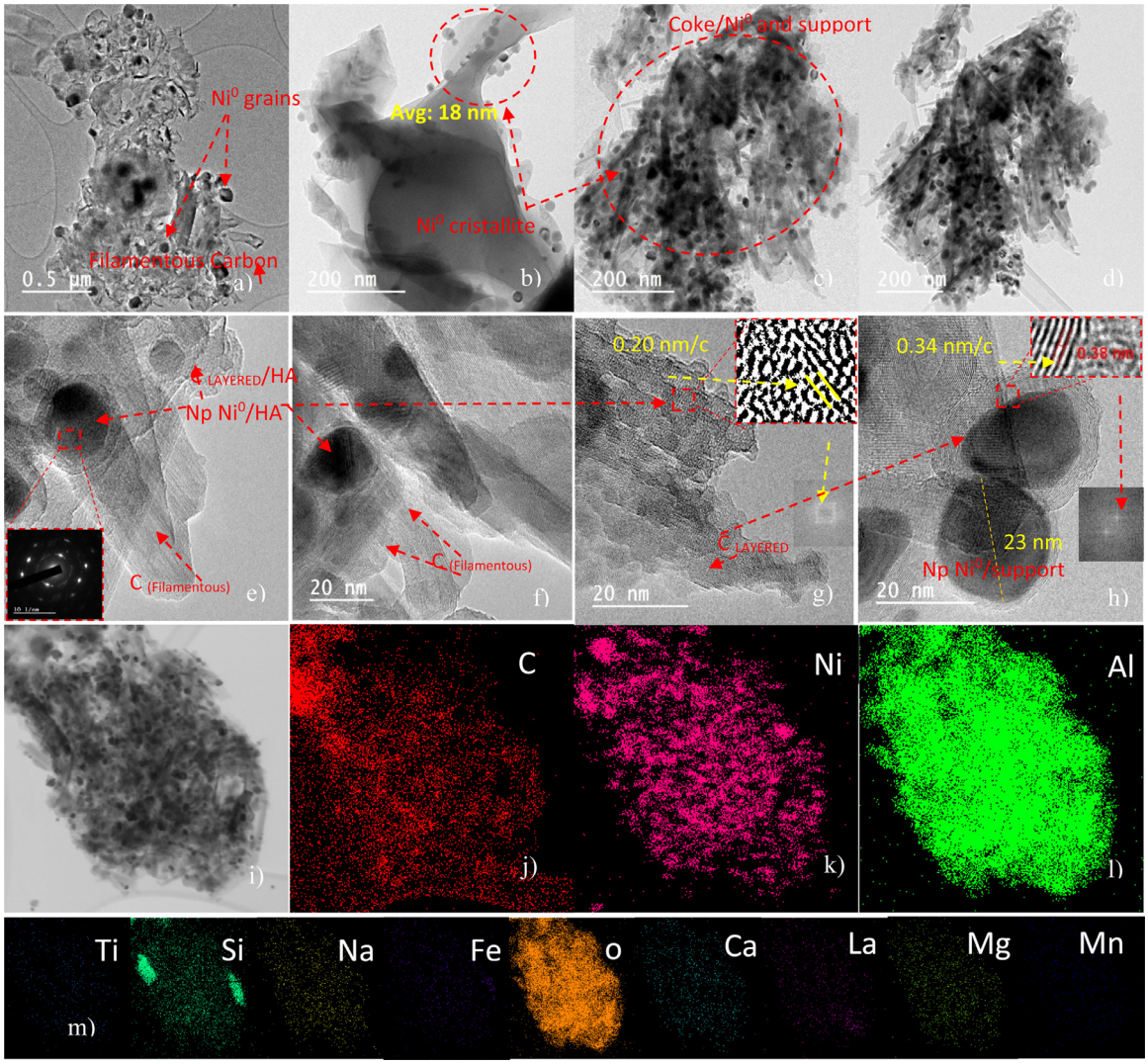

Fig. 15. TEM images and EDS mapping for *S4* after DRM for 20 h. Metallic nickel grains on the microstructure of hexaaluminates [a), b), c), d)]. Nickel cluster with coke deposits [e) f) g) h)]. TEM-EDS mapping for nickel cluster [i), j), k), l), m)].

phases in the polycrystalline regions of the different catalysts, are summarized in Table S8. Identification was performed in the planes of the observed hexaaluminates, and their correspondence with the rings of the possible phases, as a complementary analysis of the HR-TEM images, are presented in Figs. 14–16. In the case of *S1*, a better definition of the characteristic patterns, in which large points correspond to HA with very well-defined rings, was found. This result allows a better approximation in terms of determination of the interplanar distance, and also allows the carbon phase of graphite to be observed in almost all the HA planes identified, along with the Ni^0 in planes (0 3 0), (0 2 7), (0 1 3). More phases, such as Ni and NiAl present in the rings of the planes of the support, can be identified in *S2* and *S3*. This result coincides with the greater dispersion observed and a smaller grain size of the Ni^0 particles with respect to those observed in *S1*. As such, in addition to a better interaction of the metal with the support and a lower diffusion of NiO on the surface of the catalyst, all the phases in which nickel is found, and the carbon phase, can also be identified. It can therefore be assumed that the increase in nickel particles results in a higher activity compared to *S1*, which is lower due to the carbon deposits formed. In the case of *S4*, several Ni/HA phases can be observed, although the carbon phase present in the corresponding planes could not be identified. Consequently, performing a similar analysis to above, it can be assumed that this result is partially responsible for the better performance of this catalyst, and that this may be the product of a greater porosity and distribution of nickel particles in the support, a greater interaction with respect to *S1*, very similar to *S2* and *S3* and, therefore, a higher resistance to deactivation.

4. Conclusion

This study has demonstrated that it is possible to use aluminum saline slags to synthesize materials with a hexaaluminate type structure as support for Ni catalysts. The trace metals resulting from acid extraction of Al from the slag contribute positively to synthesis of the hexaaluminates since they allow an La-HA structure with an La:Al stoichiometric ratio of 1:11 to be obtained.

The hexaaluminates obtained from valorization of the aluminum saline slags and modified with Ni have been found to be active in the dry reforming of methane (DRM), with an effect of their textural properties, dispersion of the metallic phase and metal-support interaction on the performance of the catalyst in the reaction being observed. *S4* was found to be the catalyst, exhibiting the best stability and catalytic performance during the 20 h of reaction, followed by *S3, S2*, and *S1*.

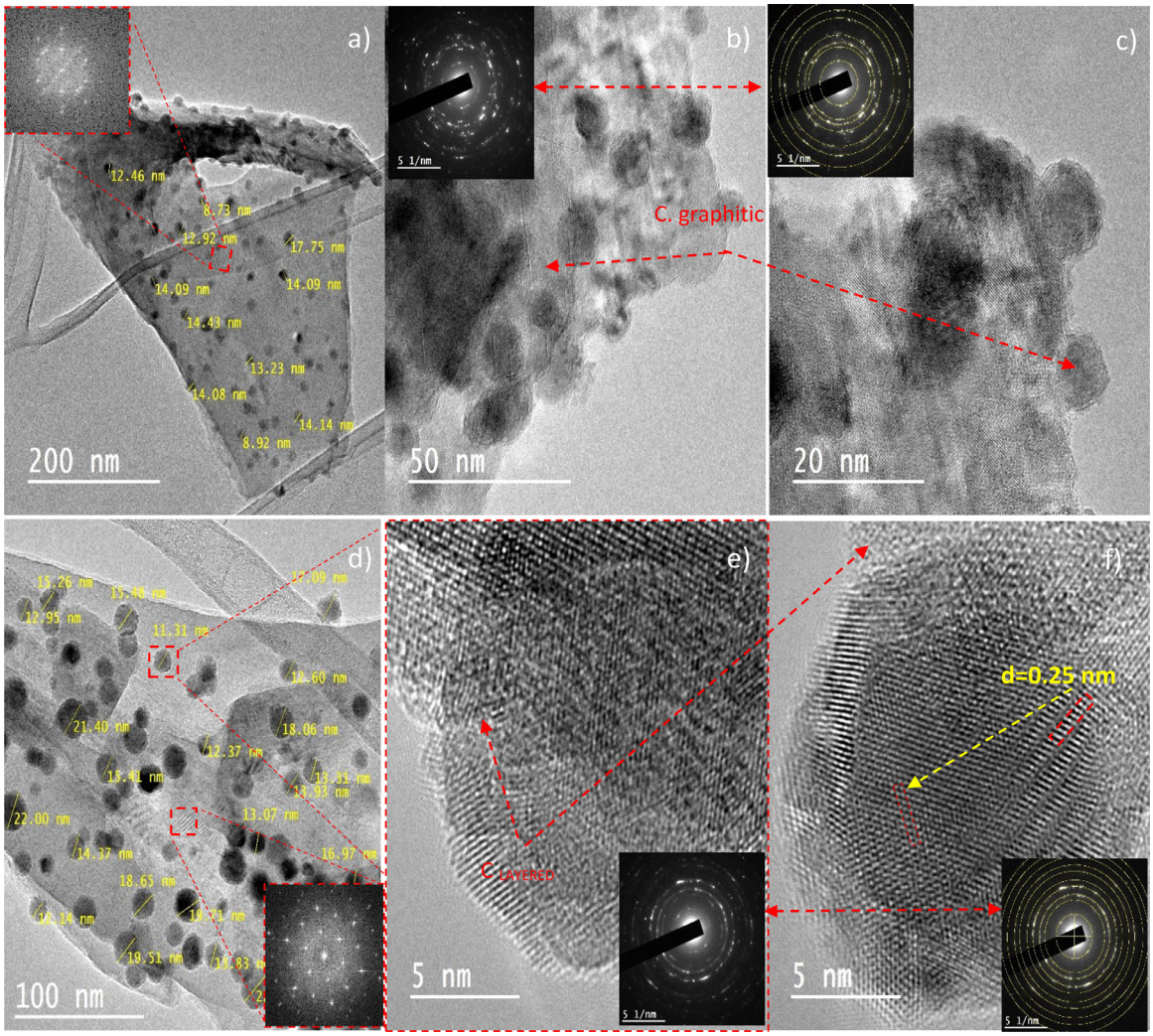

Fig. 16. TEM images and EDS mapping for *S2* and *S3* after DRM for 20 h. Distribution of metallic nickel particles on the microstructure covered by graphitic carbon in the hexaaluminate support [a), b), c)] for *S2*. Distribution of metallic nickel particles on the microstructure covered by layered carbon filament in hexaaluminates [d), e), f)] for *S3*. The boxes are the network patterns of the support [boxes a), d)], and patterns obtained by SAED of the catalyst [boxes b), c), e), f)].

Another important aspect highlighted in this work is that the purity and crystallinity of the hexaaluminate affects the interaction between the support and the metal, thus resulting in low dispersion and a very large metal grain size, which influences the performance of the reaction as fewer active sites are generated in the catalyst. It is therefore advisable to maintain a compound phase that allows a greater metal-support interaction in the case of hexaaluminate-based catalysts.

Declaration of Competing Interest

The authors declare no conflict of interest.

Acknowledgements

The authors are grateful for financial support from the Spanish Ministry of Economy, Industry and Competitiveness (AEI/MINECO), the European Regional Development Fund (ERDF) through project MAT2016-78863-C2-R. JJTH thanks Universidad Pública de Navarra for a predoctoral grant. AG also thanks Santander Bank for funding via the Research Intensification Program.

Author contributions

All the authors conceived, designed, and performed the experiments, analyzed the data, and drafted the manuscript.

Supplementary materials

Supplementary material associated with this article can be found, in the online version, at doi:10.1016/j.ceja.2020.100080.

References

[1] M. Usman, W.M.A. Wan Daud, H.F. Abbas, Dry reforming of methane: influence of process parameters—a review, Renew. Sustain. Energy Rev. 45 (2015) 710–744, doi:10.1016/j.rser.2015.02.026.
[2] R.O. Yusuf, Z.Z. Noor, A.H. Abba, M.A.A. Hassan, M.F.M. Din, Methane emission by sectors: a comprehensive review of emission sources and mitigation methods, Renew. Sustain. Energy Rev. 16 (2012) 5059–5070, doi:10.1016/j.rser.2012.04.008.
[3] Z.Z. Noor, R.O. Yusuf, A.H. Abba, M.A. Abu Hassan, M.F. Mohd Din, An overview for energy recovery from municipal solid wastes (MSW) in Malaysia scenario, Renew. Sustain. Energy Rev. 20 (2013) 378–384, doi:10.1016/j.rser.2012.11.050.
[4] H. Er-rbib, C. Bouallou, F. Werkoff, Dry reforming of methane - review of feasibility studies, Chem. Eng. Trans. 29 (2012) 163–168, doi:10.3303/CET1229028.
[5] B. Steinhauer, M.R. Kasireddy, J. Radnik, A. Martin, Development of Ni-Pd bimetallic catalysts for the utilization of carbon dioxide and methane by dry reforming, Appl. Catal. A Gen. 366 (2009) 333–341, doi:10.1016/j.apcata.2009.07.021.

[6] A.F. Lucrédio, J.M. Assaf, E.M. Assaf, Reforming of a model biogas on Ni and Rh–Ni catalysts: effect of adding La, Fuel Process. Technol. 102 (2012) 124–131, doi:10.1016/j.fuproc.2012.04.020.

[7] A. Abdulrasheed, A.A. Jalil, Y. Gambo, M. Ibrahim, H.U. Hambali, M.Y. Shahul Hamid, A review on catalyst development for dry reforming of methane to syngas: recent advances, Renew. Sustain. Energy Rev. 108 (2019) 175–193, doi:10.1016/j.rser.2019.03.054.

[8] D.B. Pal, R. Chand, S.N. Upadhyay, P.K. Mishra, Performance of water gas shift reaction catalysts: a review, Renew. Sustain. Energy Rev. 93 (2018) 549–565, doi:10.1016/j.rser.2018.05.003.

[9] B. Abdullah, N.A. Abd Ghani, D.V.N. Vo, Recent advances in dry reforming of methane over Ni-based catalysts, J. Clean. Prod. 162 (2017) 170–185, doi:10.1016/j.jclepro.2017.05.176.

[10] A. Serrano-Lotina, L. Daza, Influence of the operating parameters over dry reforming of methane to syngas, Int. J. Hydrog. Energy. 39 (2014) 4089–4094, doi:10.1016/j.ijhydene.2013.05.135.

[11] M.K. Nikoo, N.A.S. Amin, Thermodynamic analysis of carbon dioxide reforming of methane in view of solid carbon formation, Fuel Process. Technol. 92 (2011) 678–691, doi:10.1016/j.fuproc.2010.11.027.

[12] J.M. Ginsburg, J. Piña, T. El Solh, H.I. de Lasa, Coke formation over a nickel catalyst under methane dry reforming conditions: thermodynamic and kinetic models, Ind. Eng. Chem. Res. 44 (2005) 4846–4854, doi:10.1021/ie0496333.

[13] K. Takanabe, K. Nagaoka, K. Nariai, K. Aika, Titania-supported cobalt and nickel bimetallic catalysts for carbon dioxide reforming of methane, J. Catal. 232 (2005) 268–275, doi:10.1016/j.jcat.2005.03.011.

[14] G. Jones, J.G. Jakobsen, S.S. Shim, J. Kleis, M.P. Andersson, J. Rossmeisl, F. Abild-Pedersen, T. Bligaard, S. Helveg, B. Hinnemann, J.R. Rostrup-Nielsen, I. Chorkendorff, J. Sehested, J.K. Nørskov, First principles calculations and experimental insight into methane steam reforming over transition metal catalysts, J. Catal. 259 (2008) 147–160, doi:10.1016/j.jcat.2008.08.003.

[15] M. Tian, X.D. Wang, T. Zhang, Hexaaluminates: a review of the structure, synthesis and catalytic performance, Catal. Sci. Technol. 6 (2016) 1984–2004, doi:10.1039/C5CY02077H.

[16] Y. Zhang, X. Wang, Y. Zhu, X. Liu, T. Zhang, Thermal evolution crystal structure and fe crystallographic sites in LaFexAl12-xO19 hexaaluminates, J. Phys. Chem. C. 118 (2014) 10792–10804, doi:10.1021/jp500682d.

[17] P.G. De Iglesia, J.L. Menéndez, R. Torrecillas, Síntesis por sol-gel de hexaluminato de calcio, in: Proceedings of the 50 Congress SECV, Madrid, Spain., SECV, 2010, pp. 321–324. http://www.50aniversariosecv.es/Cd- libro resumenes.pdf.

[18] M. Tian, A. Wang, X. Wang, Y. Zhu, T. Zhang, Effect of large cations (La3+ and Ba2+) on the catalytic performance of Mn-substituted hexaaluminates for N_2O decomposition, Appl. Catal. B Environ. 92 (2009) 437–444, doi:10.1016/j.apcatb.2009.09.002.

[19] M. Machida, K. Eguchi, H. Arai, Catalytic properties of $BaMAl_{11}O_{19}$-α (M = Cr, Mn, Fe, Co, and Ni) for high-temperature catalytic combustion, J. Catal. 120 (1989) 377–386, doi:10.1016/0021-9517(89)90277-7.

[20] Z. Xu, M. Zhen, Y. Bi, K. Zhen, Catalytic properties of Ni modified hexaaluminates $LaNiyAl_{12-y}O_{19-\delta}$ for CO_2 reforming of methane to synthesis gas, Appl. Catal. A Gen. 198 (2000) 267–273, doi:10.1016/S0926-860X(99)00518-9.

[21] K. Zhang, G. Zhou, J. Li, K. Zhen, T. Cheng, Effective additives of A (Ce, Pr) in modified hexaaluminate LaxA1-X $NiAl_{11}O_{19}$ for carbon dioxide reforming of methane, Catal. Letters. 130 (2009) 246–253, doi:10.1007/s10562-009-9876-3.

[22] J.J. Torrez-Herrera, S.A. Korili, A. Gil, Progress in the synthesis and applications of hexaaluminate-based catalysts, Catal. Rev. (2020) 1–39 in press, doi:10.1080/01614940.2020.1831756.

[23] A. Gil, S.A. Korili, Management and valorization of aluminum saline slags: current status and future trends, Chem. Eng. J. 289 (2016) 74–84, doi:10.1016/j.cej.2015.12.069.

[24] B.R. Das, B. Dash, B.C. Tripathy, I.N. Bhattacharya, S.C. Das, Production of η-alumina from waste aluminium dross, Miner. Eng. 20 (2007) 252–258, doi:10.1016/j.mineng.2006.09.002.

[25] B. Dash, B.R. Das, B. Tripathy, I. Bhattacharya, S.C. Das, Acid dissolution of alumina from waste aluminium dross, in: Hydrometallurgy, 2008, pp. 48–53, doi:10.1016/j.hydromet.2008.01.006.

[26] J.K.H. Park, H. Lee, A processing for recycling of the domestic aluminum dross, in: Proceedings of the Global Symposium on Recycling, Waste Treatment and Clean Technology, REWAS, San Sebastian, Spain, 1999, p. 995. Vol. II.

[27] E.A. El-Katatny, S.A. Halawy, M.A. Mohamed, M.I. Zaki, Surface composition, charge and texture of active alumina powders recovered from aluminum dross tailings chemical waste, Powder Technol. 132 (2003) 137–144, doi:10.1016/S0032-5910(03)00047-0.

[28] A. López-Delgado, F. López, L. Delgado, S. López-Andrés, F.J. Priego, Study by DTA/TG of the formation of calcium aluminate obtained from an aluminium hazardous waste, J. Therm. Anal. Calorim. (2010) 99, doi:10.1007/s10973-009-0597-z.

[29] A. López-Delgado, H. Tayibi, C. Pérez, F.J. Alguacil, F.A. López, A hazardous waste from secondary aluminium metallurgy as a new raw material for calcium aluminate glasses, J. Hazard. Mater. 165 (2009) 180–186, doi:10.1016/j.jhazmat.2008.09.124.

[30] E. Ewais, N.M. Khalil, M. Amin, Y. Ahmed, M. Barakat, Utilization of aluminum sludge and aluminum slag (dross) for the manufacture of calcium aluminate cement, Ceram. Int. - CERAM INT. 35 (2009) 3381–3388, doi:10.1016/j.ceramint.2009.06.008.

[31] S. De, A.M. Balu, J.C. Van Der Waal, R. Luque, Biomass-derived porous carbon materials: synthesis and catalytic applications, ChemCatChem 7 (2015) 1608–1629, doi:10.1002/cctc.201500081.

[32] F. Teng, P. Xu, Z. Tian, G. Xiong, Y. Xu, Z. Xu, L. Lin, Synthesis of the high-surface-area CexBa1-xMnAl_{11}Oy catalyst in reverse microemulsions using inexpensive inorganic salts as precursors, Green Chem. 7 (2005) 493–499, doi:10.1039/b417229a.

[33] A. Abdulrasheed, A.A. Jalil, Y. Gambo, M. Ibrahim, H.U. Hambali, M.Y. Shahul Hamid, A review on catalyst development for dry reforming of methane to syngas: recent advances, Renew. Sustain. Energy Rev. 108 (2019) 175–193, doi:10.1016/j.rser.2019.03.054.

[34] J.R. Rostrupnielsen, J.H.B. Hansen, CO_2-reforming of methane over transition metals, J. Catal. 144 (1993) 38–49, doi:10.1006/jcat.1993.1312.

[35] L. Santamaría, F. Devred, E.M. Gaigneaux, M.A. Vicente, S.A. Korili, A. Gil, Effect of the surface properties of Me^{2+}/Al layered double hydroxides synthesized from aluminum saline slag wastes on the adsorption removal of drugs, Microporous Mesoporous Mater. 309 (2020) 110560, doi:10.1016/j.micromeso.2020.110560.

[36] J. Kim, K. Biswas, K.-.W. Jhon, S.-.Y. Jeong, W.-.S. Ahn, Synthesis of $AlPO_4$-5 and CrAPO-5 using aluminum dross, J. Hazard. Mater. 169 (2009) 919–925, doi:10.1016/j.jhazmat.2009.04.035.

[37] N. Murayama, N. Okajima, S. Yamaoka, H. Yamamoto, J. Shibata, Hydrothermal synthesis of $AlPO_4$-5 type zeolitic materials by using aluminum dross as a raw material, J. Eur. Ceram. Soc. 26 (2006) 459–462, doi:10.1016/j.jeurceramsoc.2005.06.022.

[38] S. Kuroki, T. Hashishin, T. Morikawa, K. Yamashita, M. Matsuda, Selective synthesis of zeolites A and X from two industrial wastes: crushed stone powder and aluminum ash, J. Environ. Manag. 231 (2019) 749–756, doi:10.1016/j.jenvman.2018.10.082.

[39] C. Belviso, A. Kharchenko, E. Agostinelli, F. Cavalcante, D. Peddis, G. Varvaro, N. Yaacoub, S. Mintova, Red mud as aluminium source for the synthesis of magnetic zeolite, Microporous Mesoporous Mater. (2018) 270, doi:10.1016/j.micromeso.2018.04.038.

[40] R.Sanchez Hernandez, A. López-Delgado, I. Padilla, R. Galindo Llorach, S. López-Andrés, One-step synthesis of NaP1, SOD and ANA from a hazardous aluminum solid waste, Microporous Mesoporous Mater. 226 (2016), doi:10.1016/j.micromeso.2016.01.037.

[41] T. Hiraki, A. Nosaka, N. Okinaka, T. Akiyama, Synthesis of Zeolite-X from waste metals, ISIJ Int. 49 (2009) 1644–1648, doi:10.2355/isijinternational.49.1644.

[42] M. Yoldi, E.G. Fuentes-Ordoñez, S.A. Korili, A. Gil, Zeolite synthesis from aluminum saline slag waste, Powder Technol. 366 (2020) 175–184, doi:10.1016/j.powtec.2020.02.069.

[43] C.C. Vidyasagar, Y. Arthoba Naik, Surfactant (PEG 400) effects on crystallinity of ZnO nanoparticles, Arab. J. Chem. 9 (2016) 507–510, doi:10.1016/j.arabjc.2012.08.002.

[44] Y. KAWASHIMA, T. HANDA, H. Takeuchi, M. OKUMURA, Effects of polyethylene glycol on the size of agglomerated crystals of phenytoin prepared by the spherical crystallization technique, Chem. Pharm. Bull. (Tokyo). 34 (1986) 3403–3407, doi:10.1248/cpb.34.3403.

[45] R.R. Rao, L. Mariappan, Combustion synthesis and characterisation of lanthanum hexa-aluminate, Adv. Appl. Ceram. 104 (2005) 268–271, doi:10.1179/174367605X62427.

[46] J.-.G. Park, A.N. Cormack, Defect structures and nonstoichiometry in lanthanum hexa-aluminate, J. Eur. Ceram. Soc. 19 (1999) 2249–2256, doi:10.1016/S0955-2219(99)00123-5.

[47] J. Gao, C. Jia, J. Li, M. Zhang, F. Gu, G. Xu, Z. Zhong, F. Su, Ni/Al_2O_3 catalysts for CO methanation: effect of Al_2O_3 supports calcined at different temperatures, J. Energy Chem. 22 (2013) 919–927, doi:10.1016/S2095-4956(14)60273-4.

[48] J. Zhang, H. Xu, X. Jin, Q. Ge, W. Li, Characterizations and activities of the nanosized Ni/Al_2O_3 and Ni/La-Al_2O_3 catalysts for NH_3 decomposition, Appl. Catal. A Gen. 290 (2005) 87–96, doi:10.1016/j.apcata.2005.05.020.

[49] T.H. Gardner, J.J. Spivey, E.L. Kugler, A. Campos, J.C. Hissam, A.D. Roy, Structural characterization of Ni-substituted hexaaluminate catalysts using EXAFS, XANES, XPS, XRD, and TPR, J. Phys. Chem. C. 114 (2010) 7888–7894, doi:10.1021/jp9117634.

[50] J.M. Rynkowski, T. Paryjczak, M. Lenik, On the nature of oxidic nickel phases in NiO/γ-Al_2O_3 catalysts, Appl. Catal. A, Gen. 106 (1993) 73–82, doi:10.1016/0926-860X(93)80156-K.

[51] W.-.S. Dong, H.-.S. Roh, K.-.W. Jun, S.-.E. Park, Y.-.S. Oh, Methane reforming over Ni/Ce-ZrO_2 catalysts: effect of nickel content, Appl. Catal. A Gen. 226 (2002) 63–72, doi:10.1016/S0926-860X(01)00883-3.

[52] R. Molina, Poncelet, α-Alumina-supported nickel catalysts prepared from nickel acetylacetonate: a TPR study, J. Catal. 173 (1998) 257–267, doi:10.1006/jcat.1997.1931.

[53] W. Chu, W. Yang, L. Lin, Selective oxidation of methane to syngas over NiO/Barium hexaaluminate, Catal. Lett. 74 (2001) 139–144, doi:10.1023/A:1016622301743.

[54] H. Knözinger, Temperature-programmed reduction, Handb. Heterog. Catal. 2 (1997) 676.

[55] A. Tarfaoui, Modelling the Kinetics of Reduction By Temperature Programming, Technische Universiteit Delft Technische Universiteit Delft, The Netherlands, 1996 , 2020.

[56] J.M. Kanervo, A.O.I. Krause, Kinetic analysis of temperature-programmed reduction: behavior of a CrOx/Al_2O_3 catalyst, J. Phys. Chem. B. 105 (2001) 9778–9784, doi:10.1021/jp0114079.

[57] W. Tao, H. Cheng, W. Yao, X. Lu, Q. Zhu, G. Li, Z. Zhou, Syngas production by CO_2 reforming of coke oven gas over Ni/La_2O_3-ZrO_2 catalysts, Int. J. Hydrog. Energy. 39 (2014) 18650–18658, doi:10.1016/j.ijhydene.2014.02.029.

[58] S. Sokolov, E.V. Kondratenko, M.M. Pohl, A. Barkschat, U. Rodemerck, Stable low-temperature dry reforming of methane over mesoporous La_2O_3-ZrO_2 supported Ni catalyst, Appl. Catal. B Environ. 113–114 (2012) 19–30, doi:10.1016/j.apcatb.2011.09.035.

[59] Z. Li, L. Mo, Y. Kathiraser, S. Kawi, Yolk-satellite-shell structured Ni-Yolk@Ni@SiO_2 nanocomposite: superb catalyst toward methane CO_2 reforming reaction, ACS Catal. 4 (2014) 1526–1536, doi:10.1021/cs401027p.

[60] S.C. Tsang, J.B. Claridge, M.L.H. Green, Recent advances in the conversion of methane to synthesis gas, Catal. Today. 23 (1995) 3–15, doi:10.1016/0920-5861(94)00080-L.
[61] J.H. Edwards, A.M. Maitra, The chemistry of methane reforming with carbon dioxide and its current and potential applications, Fuel Process. Technol. 42 (1995) 269–289, doi:10.1016/0378-3820(94)00105-3.
[62] D. San José-Alonso, M.J. Illán-Gómez, M.C. Román-Martínez, Low metal content Co and Ni alumina supported catalysts for the CO_2 reforming of methane, Int. J. Hydrog. Energy. 38 (2013) 2230–2239, doi:10.1016/j.ijhydene.2012.11.080.
[63] J. Zhang, H. Wang, A.K. Dalai, Development of stable bimetallic catalysts for carbon dioxide reforming of methane, J. Catal. 249 (2007) 300–310, doi:10.1016/j.jcat.2007.05.004.
[64] G. Zhang, J. Liu, Y. Xu, Y. Sun, A review of CH_4–CO reforming to synthesis gas over Ni-based catalysts in recent years (2010–2017), Int. J. Hydrog. Energy. 43 (2018) 15030–15054, doi:10.1016/j.ijhydene.2018.06.091.